Production spectra with a Σ^- hyperon in (π^-, K^+) reactions on light to heavy nuclei

Toru Harada[1,2,*] and Yoshiharu Hirabayashi[3]
[1]*Center for Physics and Mathematics, Osaka Electro-Communication University, Neyagawa, Osaka 572-8530, Japan*
[2]*J-PARC Branch, KEK Theory Center, Institute of Particle and Nuclear Studies,*
High Energy Accelerator Research Organization (KEK), 203-1, Shirakata, Tokai, Ibaraki 319-1106, Japan
[3]*Information Initiative Center, Hokkaido University, Sapporo 060-0811, Japan*

(Received 26 August 2022; revised 8 April 2023; accepted 25 April 2023; published 19 May 2023)

We study theoretically production spectra with a Σ^- hyperon via (π^-, K^+) reactions on ^{12}C, ^{28}Si, ^{58}Ni, ^{115}In, and ^{209}Bi targets, using the Green's function method in the framework of a distorted-wave impulse approximation with the optimal Fermi averaging for an elementary $\pi^- p \to K^+\Sigma^-$ t matrix. Adopting distorted waves obtained by solving a Klein-Gordon equation for π^- and K^+ mesons, we improve and update the calculated spectra of Σ^- production cross sections comprehensively in comparison with the data of the KEK-E438 experiment. We use several Σ-nucleus (optical) potentials that are determined by fits to the Σ^- atomic data and that take into account the energy dependence arising from the nuclear excitation via $\Sigma N \to \Sigma N$ scatterings with a Σ hyperon effective mass. The results show that the absolute values and the shapes of these calculated spectra are in excellent agreement with those of the data, so that a mass-number dependence of integrated cross sections on the light-to-heavy targets is well reproduced in our calculations. It confirms that the Σ-nucleus potentials having a repulsion inside the nuclear surface and an attraction outside the nucleus with a sizable absorption are favored in reproducing the data of the nuclear (π^-, K^+) spectra and the Σ^- atomic x ray simultaneously, whereas it is still difficult to determine the radial distribution of the Σ-nucleus potential inside the nucleus and its strength at the center.

DOI: 10.1103/PhysRevC.107.054611

I. INTRODUCTION

A Σ hyperon in nuclei is one of the most interesting subjects used to understand the behavior of strangeness in nuclear medium in hypernuclear physics [1]. Noumi and his collaborators [2,3] performed measurements of Σ^- hypernuclei by inclusive (π^-, K^+) reactions on C, Si, Ni, In, and Bi targets at the incident laboratory momentum $p_{\text{lab}} = 1.2$ GeV/c in the KEK-E438 experiment. Their analysis in a distorted-wave impulse approximation (DWIA) suggested that the Σ-nucleus potential has a strong repulsion in the real part and a sizable absorption in the imaginary part [2,3]. This repulsion may be caused by the ΣN $I = 3/2$, $^3S_1$ channel [4–6], in which a quark Pauli-forbidden state occurs in a baryon-baryon system [7], as supported by modern YN potentials [8] and recent lattice QCD calculations [9,10]. The behavior of the Σ^- hyperon in nuclear medium affects the maximal mass of neutron stars, in which a baryon fraction would depend on the properties of hypernuclear potentials for neutron stars in astrophysics [11,12].

In previous papers [13,14], we succeeded in explaining the data of the (π^-, K^+) reactions on ^{28}Si and ^{209}Bi targets at 1.2 GeV/c, estimating Σ^- production spectra in the quasifree (QF) region in the DWIA with optimal Fermi averaging [15] for an elementary $\pi^- p \to K^+\Sigma^-$ t matrix. We showed that the Σ-nucleus potentials have a repulsion inside the nuclear surface and an attraction outside the nucleus with a sizable absorption, as suggested by the latest studies of the Σ^- atomic x ray [13,14,16–20]. Our analysis [13,14] also indicated that the Σ-nucleus potential within the Woods-Saxon (WS) or 2pF form is

$$U_\Sigma(r) = \left(V_0^\Sigma + iW_0^\Sigma\right)/[1 + \exp\{(r - R)/a\}] \qquad (1)$$

with $R = 1.1A_{\text{core}}^{1/3}$ and $a = 0.67$ fm, where $V_0^\Sigma =$ (+20)–(+30) MeV and $W_0^\Sigma =$ (−20)–(−40) MeV, corresponding to a strong repulsion in the real part and a sizable absorption in the imaginary part of the potential [21]. Such a Σ-nucleus potential [22] explains the spectra for Σ^--^{5}He in the ^{6}Li(π^-, K^+) data at the J-PARC E10 experiment [23].

However, it should be noted that the absolute values of the calculated cross sections of the (π^-, K^+) reactions on medium-to-heavy nuclei were by a factor of 2–4 larger than those of the data in the DWIA with an eikonal approximation for meson distorted waves [13,14]. Figure 1 shows the mass number A dependence of the integrated cross sections $\sigma(^A\text{Z})$ from C up to Bi targets at $p_{\text{lab}} = 1.2$ GeV/c and $\theta_{\text{lab}} = 6°$, which was calculated from Refs. [13,14] using the eikonal approximation. As shown by Saha *et al.* [3], the magnitudes of the calculated Σ^- production cross sections in the eikonal approximation are rather steeper than those of the data, as a function of the mass number A. This discrepancy may require an improvement of the eikonal DWIA for precisely estimating the Σ^- production in the nuclear (π^-, K^+) reactions. Kohno *et al.* [24,25] analyzed the same QF

---

[*] harada@osakac.ac.jp

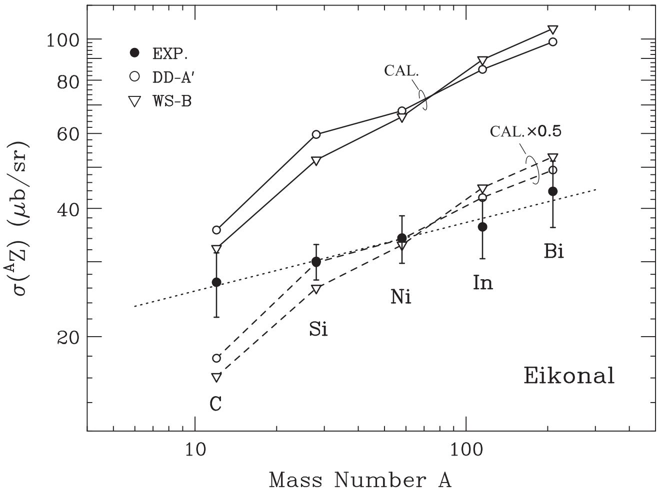

FIG. 1. Mass-number A dependence of the integrated cross sections $\sigma(^{A}\mathrm{Z})$ from C up to Bi targets at $p_{\rm lab} = 1.2$ GeV/c and $\theta_{\rm lab} = 6^\circ$. The experimental data are obtained from Ref. [3]. Dotted lines denote $C \times A^{0.161}$ for an eye guide to the data where C is a constant. Solid lines indicate the calculated results (CAL.) with the Σ-nucleus potentials for DD-A′ and WS-B in the eikonal approximation [13,14], and dashed lines indicate results multiplied by a scaling factor of 0.5 in order to be compared with the slope of the data.

data of the ^{28}Si(π^-, K^+) reaction using the semiclassical distorted-wave (SCDW) model with distorted waves obtained by solving a Klein-Gordon equation for π^- and K^+. Their analysis also suggests the repulsive nature of $V_0^\Sigma \simeq$ (+30)-(+50) MeV in a WS form with $R = 3.60$ fm, $a = 0.60$ fm, and $W_0^\Sigma = -20$ MeV, whereas their calculated spectra seem to be insufficient to reproduce those of the data. Consequently, more quantitative improvements are needed for the DWIA calculations.

In this paper, we study theoretically the Σ^- production spectra in the (π^-, K^+) reactions on ^{12}C, ^{28}Si, ^{58}Ni, ^{115}In, and ^{209}Bi targets at $p_{\rm lab} = 1.2$ GeV/c, using the DWIA framework with the optimal Fermi averaging [15] for the $\pi^- p \to K^+\Sigma^-$ t matrix. To evaluate the full distortions for π^- and K^+ mesons, we estimate the distorted waves obtained by solving a Klein-Gordon equation for these mesons. Thus we improve and update the calculated spectra comprehensively in comparison with the data of the KEK-E438 experiment, using the Σ-nucleus potentials that are determined by fits to the Σ^- atomic data and by considering the energy dependence arising from the nuclear excitation via $\Sigma N \to \Sigma N$ scatterings with a Σ hyperon effective mass. We also discuss the mass-number dependence on the integrated cross section of the nuclear (π^-, K^+) reactions, which depends on the distortion effects and the nature of the Σ-nucleus potentials in our analysis.

II. THEORETICAL PROCEDURES

A. Distorted-wave impulse approximation

We briefly mention a calculation procedure of hypernuclear production via the nuclear (π^-, K^+) reaction in the distorted-wave impulse approximation (DWIA) with the optimal Fermi averaging [15] for the elementary $\pi^- p \to K^+\Sigma^-$ t matrix. The inclusive double differential cross section [26,27] in the laboratory frame is given by (in units $\hbar = c = 1$)

$$\frac{d^2\sigma}{dE_K d\Omega_K} = \beta \frac{1}{[J_A]} \sum_{m_A} \sum_{B} |\langle \Psi_B|\hat{F}|\Psi_A\rangle|^2 \times \delta(E_K + E_B - E_\pi - E_A), \qquad (2)$$

where $[J] = 2J + 1$, and E_K, E_π, E_B, and E_A are the energies of outgoing K^+, incoming π^-, hypernuclear states, and the target nucleus, respectively. Ψ_B and Ψ_A are wave functions of hypernuclear final states and the initial state of the target nucleus, respectively. The kinematical factor β [28] arising from a translation from a two-body meson-nucleon laboratory system to a meson-nucleus laboratory system [29] is given by

$$\beta = \left(1 + \frac{E_K^{(0)}}{E_B^{(0)}} \frac{p_K^{(0)} - p_\pi^{(0)} \cos\theta_{\rm lab}}{p_K^{(0)}}\right) \frac{p_K E_K}{p_K^{(0)} E_K^{(0)}}, \qquad (3)$$

where $p_\pi^{(0)}$ and $p_K^{(0)}$ ($E_K^{(0)}$ and $E_B^{(0)}$) are laboratory momenta of π^- and K^+ (laboratory energies of K^+ and Σ^-) in the two-body $\pi^- p \to K^+\Sigma^-$ reactions, respectively. Here we consider only the non-spin-flip reaction because we are interested in the cross sections around the K^+ forward direction. Thus an external operator $\hat{F}$ for the associated production $\pi^- p \to K^+\Sigma^-$ reactions is given by

$$\hat{F} = \int d\boldsymbol{r}\, \chi^{(-)*}_{\boldsymbol{p}_K}(\boldsymbol{r}) \chi^{(+)}_{\boldsymbol{p}_\pi}(\boldsymbol{r}) \sum_{j=1}^{A} \overline{f}_{\pi^- p \to K^+\Sigma^-} \delta(\boldsymbol{r} - \boldsymbol{r}_j) \hat{O}_j, \qquad (4)$$

where we assume zero-range interaction for the $\pi^- p \to K^+\Sigma^-$ transitions. The functions $\chi^{(-)*}_{\boldsymbol{p}_K}$ and $\chi^{(+)}_{\boldsymbol{p}_\pi}$ are distorted waves of outgoing K^+ and incoming π^- mesons, respectively. $\hat{O}_j$ is a baryon operator changing jth nucleon into a Σ^- hyperon in the nucleus, and $\boldsymbol{r}$ is the relative coordinate between the mesons and the center of mass (c.m.) of the nucleus; the quantity $\overline{f}_{\pi^- p \to K^+\Sigma^-}$ is the Fermi-averaged amplitude for the $\pi^- p \to K^+\Sigma^-$ reactions in nuclei on the laboratory frame [13,22]. The energy and momentum transfer to the Σ^- final state is given by

$$\omega = E_\pi - E_K, \quad \boldsymbol{q} = \boldsymbol{p}_\pi - \boldsymbol{p}_K, \qquad (5)$$

where $E_\pi = (m_\pi^2 + \boldsymbol{p}_\pi^2)^{1/2}$ and $E_K = (m_K^2 + \boldsymbol{p}_K^2)^{1/2}$ are the laboratory energies of π^- and K^+ in the nuclear reactions, respectively; m_π and m_K ($\boldsymbol{p}_\pi$ and $\boldsymbol{p}_K$) are masses (laboratory momenta) of π^- and K^+, respectively.

The double differential cross section of Eq. (2) is often approximated as

$$\frac{d^2\sigma}{dE_K d\Omega_K} = \left(\frac{d\sigma}{d\Omega}\right)^{\rm opt} S(\omega, \boldsymbol{q}) \qquad (6)$$

in the DWIA [4,30,31], where $(d\sigma/d\Omega)^{\rm opt}$ is the in-medium $\pi^- p \to K^+\Sigma^-$ cross section, and $S(\omega, \boldsymbol{q})$ denotes the strength function describing the dynamics of the nuclear

TABLE I. Energies ϵ_N of single-particle states for a proton in ^{12}C, ^{28}Si, ^{58}Ni, ^{115}In, and ^{209}Bi targets, which are input in these calculations [34–37]. The values in parentheses denote widths of hole states for a proton. All energies and widths are in MeV.

$(n\ell j)_p$	^{12}C		^{28}Si		^{58}Ni		^{115}In		^{209}Bi	
$0s_{1/2}$	−37.0	(10.0)	−38.0	(10.0)	−41.9	(10.0)	−42.9	(10.0)	−36.6	(10.0)
$0p_{3/2}$	−18.7	(0.0)	−23.4	(6.0)	−30.8	(10.0)	−35.4	(10.0)	−33.1	(10.0)
$0p_{1/2}$			−19.1	(5.0)	−28.9	(8.0)	−34.3	(10.0)	−32.5	(10.0)
$0d_{5/2}$			−9.7	(2.0)	−19.2	(4.0)	−27.0	(6.0)	−28.4	(6.0)
$1s_{1/2}$			−6.0	(0.0)	−14.6	(2.0)	−24.4	(6.0)	−24.0	(6.0)
$0d_{3/2}$					−14.5	(2.0)	−23.1	(6.0)	−27.0	(6.0)
$0f_{7/2}$					− 7.8	(0.0)	−18.2	(4.0)	−22.9	(6.0)
$0f_{5/2}$							−13.3	(4.0)	−20.4	(4.0)
$1p_{3/2}$							−13.7	(2.0)	−17.1	(4.0)
$1p_{1/2}$							−11.6	(2.0)	−16.0	(2.0)
$0g_{9/2}$							−9.1	(0.0)	−15.4	(2.0)
$0g_{7/2}$									−11.4	(2.0)
$1d_{5/2}$									−9.7	(1.0)
$1d_{3/2}$									−9.4	(1.0)
$2s_{1/2}$									−8.4	(1.0)
$0h_{11/2}$									−8.0	(1.0)
$0h_{9/2}$									−3.8	(0.0)

states, which is written by

$$S(\omega,\boldsymbol{q}) = \frac{1}{[J_A]}\sum_{m_A,B}\left|\langle\Psi_B|\,\chi^{(-)*}_{\boldsymbol{p}_K}\chi^{(+)}_{\boldsymbol{p}_\pi}\,|\Psi_A\rangle\right|^2\delta(\omega+E_A-E_B). \tag{7}$$

For the initial states Ψ_A, we obtain single-particle wave functions for a proton in the target nucleus, using a Woods-Saxon potential [32],

$$U_N(r) = V_0^N f(r) + V_{ls}^N(\boldsymbol{l}\cdot\boldsymbol{s})r_0^2\frac{1}{r}\frac{d}{dr}f(r) \tag{8}$$

with

$$f(r) = [1+\exp\{(r-R)/a\}]^{-1}, \tag{9}$$

where $V_{ls}^N = -0.44V_0^N$, $a = 0.67$ fm, $r_0 = 1.27$ fm, and $R = r_0A^{1/3}$, adjusting the strength of V_0^N to reproduce the data of the charge radius [33,34]; we have $V_0^N = -64.8$, -63.1, -59.0, -58.4, and -61.7 MeV for ^{12}C, ^{28}Si, ^{58}Ni, ^{115}In, and ^{209}Bi, fitting to the charge root-mean radius of $\langle r^2\rangle^{1/2}_{\rm ch} = 2.44$, 3.10, 3.77, 4.59, and 5.52 fm, respectively. The Coulomb potential for a proton is used with a uniform distribution of a charged sphere where the radius $R_C = 1.2A^{1/3}$. In Table I, we list energies ϵ_N of single-particle states for a proton in the target nuclei, which are input in these calculations, and widths for these hole states are taken from $(e, e'p)$ experimental data [34,35]. For deeply hole states of which energies are unknown experimentally, theoretical predictions with a density-dependent Hartree-Fock method [36,37] are used.

B. Green's function method

For final states Ψ_B, we use the Green's function method [31] to examine not only bound states but also continuum states for a Σ^- hyperon, so as to evaluate the strength function $S(\omega,\boldsymbol{q})$. The complete Green's function G provides all information concerning Σ-nucleus dynamics as a function of the energy transfer $\omega = E_B - E_A$ corresponding to the energy E measured from the Σ^- + core-nucleus threshold,

$$E = E_B - (m_{\Sigma^-} + M_C) = -B_{\Sigma^-}, \tag{10}$$

where m_{Σ^-} hyperon and M_C are masses of the Σ^- hyperon and the core nucleus, respectively. It is obtained by solving the following potential problems:

$$G(\omega) = G^{(0)}(\omega) + G^{(0)}(\omega)\{U_\Sigma + U_{\rm Coul}\}G(\omega), \tag{11}$$

where $G^{(0)}$ is a free Green's function, U_Σ is the Σ^--nucleus potential, and $U_{\rm Coul}$ is the finite Coulomb potential between the Σ^- hyperon and the core nucleus. By the use of a complete Green's function G, a sum of the final states B of Eq. (2) is given as

$$\sum_B|\Psi_B\rangle\delta(\omega+E_A-E_B)\langle\Psi_B| = -\frac{1}{\pi}{\rm Im}\,G(\omega). \tag{12}$$

Thus the strength function $S(\omega,\boldsymbol{q})$ is estimated by

$$S(\omega,\boldsymbol{q}) = -\frac{1}{\pi}{\rm Im}\sum_{\alpha\alpha'}\int d\boldsymbol{r}\,d\boldsymbol{r}'F_\Sigma^{\alpha\,\dagger}(\boldsymbol{r})G_\Sigma^{\alpha\alpha'}(\omega;\boldsymbol{r},\boldsymbol{r}')F_\Sigma^{\alpha'}(\boldsymbol{r}'), \tag{13}$$

where $G_\Sigma^{\alpha\alpha'}$ is a complete Green's function [31] for Σ hypernuclear final states, and α (α') denotes the complete set of eigenstates for the system. The function F_Σ^α is a Σ production amplitude, which is written as

$$F_\Sigma^\alpha(\boldsymbol{r}) = \chi^{(-)*}_{\boldsymbol{p}_K}(\boldsymbol{r})\chi^{(+)}_{\boldsymbol{p}_\pi}(\boldsymbol{r})\langle\alpha\,|\hat{\psi}_N(\boldsymbol{r})|\,\Psi_A\rangle, \tag{14}$$

where $\langle\alpha\,|\hat{\psi}_N(\boldsymbol{r})|\Psi_A\rangle$ is a hole-state wave function for a struck nucleon in the target.

C. Optimal Fermi averaging

To evaluate the $\pi^- p \to K^+\Sigma^-$ reaction in nuclear medium, we deal with the optimal Fermi averaging (OFA) for the elementary $\pi^- p \to K^+\Sigma^-$ t matrix [15]. We obtain the "optimal" differential cross sections of the in-medium $\pi^- p \to K^+\Sigma^-$ reactions in the nucleus [13] to fully describe the energy (ω) dependence of the nuclear (π^-, K^+) reactions, where N^* resonances as intermediate states may be populated in the $\pi^- p \to K^+\Sigma^-$ processes. This differential cross section is written by

$$\left(\frac{d\sigma}{d\Omega}\right)^{\rm opt} = \beta|\overline{f}_{\pi^- p\to K^+\Sigma^-}|^2, \tag{15}$$

where the Fermi-averaged amplitude $\overline{f}_{\pi^- p\to K^+\Sigma^-}$ is given by

$$\overline{f}_{\pi^- p\to K^+\Sigma^-} = -\frac{1}{2\pi}\left(\frac{p_K E_K E_\pi}{\beta p_\pi}\right)^{1/2} t^{\rm opt}_{\pi N, K\Sigma}(p_\pi;\omega,\boldsymbol{q}). \tag{16}$$

The quantity $t^{\rm opt}_{\pi N,K\Sigma}$ is the optimal Fermi-averaged $\pi^- p \to K^+\Sigma^-$ t matrix, which is defined as

$$t^{\rm opt}_{\pi N,K\Sigma}(p_\pi;\omega,\boldsymbol{q}) = \left.\frac{\int_0^\pi \sin\theta_N d\theta_N \int_0^\infty dp_N p_N^2 n(p_N) t(E_{\pi N};\boldsymbol{p}_\pi,\boldsymbol{p}_N)}{\int_0^\pi \sin\theta_N d\theta_N \int_0^\infty dp_N p_N^2 n(p_N)}\right|_{\boldsymbol{p}_N=\boldsymbol{p}_N^*}, \tag{17}$$

where $t(E_{\pi N};\boldsymbol{p}_\pi,\boldsymbol{p}_N)$ is the two-body on-shell t matrix for the $\pi^- p \to K^+\Sigma^-$ reaction in free space, $E_{\pi N} = E_\pi + E_N$ is a total energy of the $\pi^- N$ system, and $\cos\theta_N = \hat{\boldsymbol{p}}_\pi \cdot \hat{\boldsymbol{p}}_N$; E_N and $\boldsymbol{p}_N$ are an energy and a momentum of the nucleon in the nucleus, respectively. The function $n(p)$ is a momentum distribution of a struck nucleon in the nucleus, normalized by $\int n(p)d\boldsymbol{p}/(2\pi)^3 = 1$. The subscript $\boldsymbol{p}_N = \boldsymbol{p}_N^*$ in Eq. (17) means the integral with a constraint imposed on the variables of (p_N, θ_N) in an on-energy-shell momentum $\boldsymbol{p}_N^*$. This momentum $\boldsymbol{p}_N^*$ is a solution that satisfies the on-energy-shell equation for a struck nucleon at the point $(\omega, \boldsymbol{q})$ in the nuclear systems,

$$\sqrt{(\boldsymbol{p}_N^* + \boldsymbol{q})^2 + m_\Sigma^2} - \sqrt{(\boldsymbol{p}_N^*)^2 + m_N^2} = \omega, \tag{18}$$

where m_Σ and m_N are masses of the Σ^- hyperon and the nucleon, respectively. Note that this procedure keeps the on-energy-shell $\pi^- p \to K^+\Sigma^-$ processes in the nucleus [38], so that it guarantees to take "optimal" values for $t^{\rm opt}_{\pi N,K\Sigma}$; binding effects for the nucleon and the Σ^- hyperon in the nucleus are considered automatically when we input experimental values for energies of the nuclear and hypernuclear states [39]. We also take into account the correction for the energies of the struck nucleons in the nucleus,

$$\omega \to \omega + \langle \Delta\epsilon_N \rangle, \tag{19}$$

where the averaged value $\langle \Delta\epsilon_N \rangle$ of the different energy distributions of their single-particle states $\varphi_N^{(i)}$ is given by

$$\langle \Delta\epsilon_N \rangle = \sum_i \left(\epsilon_N^{(i)} - \epsilon_N^{(0)}\right) Z_{\rm eff}^{(i)}/Z_{\rm eff}, \tag{20}$$

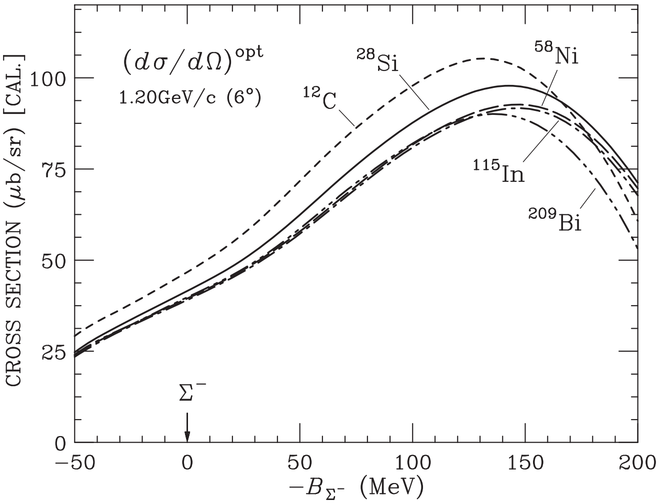

FIG. 2. Energy dependence of the optimal cross sections of $(d\sigma/d\Omega)^{\rm opt}$ in the (π^-, K^+) reactions on ^{12}C, ^{28}Si, ^{58}Ni, ^{115}In, and ^{209}Bi targets at $p_{\rm lab} = 1.2$ GeV/c and $\theta_{\rm lab} = 6°$, as a function of $-B_{\Sigma^-}$. The arrow shows the Σ^- emitted threshold.

using the effective number of protons

$$Z_{\rm eff} = \sum_i Z_{\rm eff}^{(i)}, \tag{21a}$$

$$Z_{\rm eff}^{(i)} = \int \left|\varphi_N^{(i)}(r)\right|^2 D_{\pi K}(\boldsymbol{r}) d\boldsymbol{r}, \tag{21b}$$

with a meson absorption factor $D_{\pi K}(\boldsymbol{r})$ for the nuclear (π^-, K^+) reactions (see Sec. IV B). Thus we have, e.g., $\langle \Delta\epsilon_N \rangle = -9.9$ MeV for ^{28}Si and $\langle \Delta\epsilon_N \rangle = -10.8$ MeV for ^{209}Bi. As a result, the ω dependence of $(d\sigma/d\Omega)^{\rm opt}$ is indispensable for explaining behavior of the nuclear (π^-, K^+) reactions [13].

In Fig. 2, we display the "optimal" cross sections for the Σ^--nucleus systems in the (π^-, K^+) reactions on ^{12}C, ^{28}Si, ^{58}Ni, ^{115}In, and ^{209}Bi targets, as a function of the energy $-B_{\Sigma^-}$. Here we use a momentum distribution obtained by a harmonic oscillator model,

$$n(p) = n_0\left\{N_s + \tfrac{2}{3}N_p(bp)^2 + \tfrac{4}{15}N_d(bp)^4\right\}\exp\{-(bp)^2\}, \tag{22}$$

where the size parameters $b = 1.64$ fm for ^{12}C ($N_s = 2$, $N_p = 4$, $N_d = 0$) and $b = 1.87$ fm for ^{28}Si ($N_s = 2$, $N_p = 6$, $N_d = 6$). For ^{58}Ni, ^{115}In, and ^{209}Bi, we use a Fermi distribution given by

$$n(p) = n_0[1 + \exp\{(p - p_0)/\Delta p\}]^{-1}, \tag{23}$$

where $p_0 = 100$ MeV/c and $\Delta p = 50$ MeV/c. We find that the absolute values of the optimal cross sections slightly depend on the target nucleus. This dependence comes from a difference among the single-particle energies in the targets, by solving the on-energy-shell equation of Eq. (18) in the OFA procedure, though the optimal cross sections are insensitive to the momentum distributions $n(p)$, as discussed in Ref. [4]. Therefore, we recognize that it is important to take into account the binding effects in the nucleus.

D. Distorted waves for mesons

The distorted waves for the incoming π^- and outgoing K^+ mesons in Eq. (4) are written by the partial wave expansion in the z axis as the direction of the incident π^- laboratory momentum $\boldsymbol{p}_\pi$,

$$\chi^{(-)*}_{\boldsymbol{p}_K}(\boldsymbol{r})\chi^{(+)}_{\boldsymbol{p}_\pi}(\boldsymbol{r}) = \sum_{LM}\sqrt{4\pi(2L+1)}\,i^L\tilde{j}_{LM}(\theta_{\rm lab},r)Y_{LM}(\hat{\boldsymbol{r}}), \tag{24}$$

where $\tilde{j}_{LM}(\theta_{\rm lab},r)$ is a radial distorted wave with the angular momentum with (L, M),

$$\begin{aligned}\tilde{j}_{LM}(\theta_{\rm lab},r) &= \sum_{\ell_a\ell_b}(-)^{(\ell_a-\ell_b-L)/2}(2\ell_a+1)(2\ell_b+1)\\ &\quad\times\tilde{j}^*_{\ell_b}\left(\frac{M_C}{M_B}r\right)\tilde{j}_{\ell_a}\left(\frac{M_C}{M_A}r\right)\\ &\quad\times\begin{pmatrix}\ell_a & \ell_b & L\\ 0 & 0 & 0\end{pmatrix}\begin{pmatrix}\ell_a & \ell_b & L\\ 0 & M & -M\end{pmatrix}\hat{Y}_{\ell_bM}(\hat{\boldsymbol{p}}_K),\end{aligned} \tag{25}$$

and $\theta_{\rm lab}$ is the scattering angle to the forward direction in the nuclear (π^-, K^+) reaction. The functions $\tilde{j}_{\ell_a}(r)$ and $\tilde{j}_{\ell_b}(r)$ are the radial distorted waves for π^- and K^+, respectively. The factors of M_C/M_A and M_C/M_B arise from the recoil correction, where M_A, M_B and M_C are the masses of the target, the hypernucleus, and the core nucleus, respectively. The function $\hat{Y}$ is defined by $\hat{Y}_{\ell_bM}(\hat{\boldsymbol{p}}_K) = Y_{\ell_bM}(\hat{\boldsymbol{p}}_K)(4\pi/2\ell_b+1)^{1/2}$.

In previous works [13,14], we used the computational procedure for the distorted waves in the eikonal approximation, due to the large momentum transfer $q \simeq 400$–530 MeV/c in the (π^-, K^+) reaction, where we took $\sigma_\pi = 38$ mb for the π^-N scattering and the $\sigma_K = 18$ mb for K^+N one, and $\alpha_\pi = \alpha_K = 0$, as the distortion parameters. To improve $\tilde{j}_{\ell_a}$ and $\tilde{j}_{\ell_b}$ in Eq. (25), here, we have the partial-wave expansion for the distorted waves for π^- and K^+:

$$\chi^{(+)}_{\boldsymbol{p}_\pi}(\boldsymbol{r}) = 4\pi\sum_{\ell_am_a}i^{\ell_a}\tilde{j}_{\ell_a}(r)Y_{\ell_am_a}(\hat{\boldsymbol{r}})Y^*_{\ell_am_a}(\hat{\boldsymbol{p}}_\pi), \tag{26a}$$

$$\chi^{(-)}_{\boldsymbol{p}_K}(\boldsymbol{r}) = 4\pi\sum_{\ell_bm_b}i^{\ell_b}\tilde{j}_{\ell_b}(r)Y_{\ell_bm_b}(\hat{\boldsymbol{r}})Y^*_{\ell_bm_b}(\hat{\boldsymbol{p}}_K), \tag{26b}$$

which satisfy a Klein-Gordon (KG) equation of the form [40],

$$\left[-\nabla^2 + \left\{(E^2-m^2) + 2E(U_C+U_S) - U_C^2\right\}\right]\chi^{(\pm)} = 0, \tag{27}$$

where U_C is a unified Coulomb potential with the radius of $R_C = r_CA^{1/3}$, and m is the meson mass. The optical potentials U_S for the mesons are used in the standard Kisslinger form,

$$2EU_S = -p^2\tilde{b}(r) + \nabla\cdot\tilde{c}(r)\nabla \tag{28}$$

with

$$\tilde{b}(r) = b_0\rho(r) - \epsilon b_1\delta\rho(r), \tag{29a}$$

$$\tilde{c}(r) = c_0\rho(r) - \epsilon c_1\delta\rho(r), \tag{29b}$$

where $\rho(r) = \rho_p(r) + \rho_n(r)$, $\delta\rho(r) = \rho_n(r) - \rho_p(r)$, $\epsilon = -1$ for π^-, and $\epsilon = +1$ for K^+; $\rho_p(r)$ and $\rho_n(r)$ are nuclear densities normalized to the number of protons Z and neutrons N, respectively. The quantities b_0 and c_0 (b_1 and c_1) are isoscalar (isovector) strength parameters. We obtain these parameters of the Fermi-averaged amplitudes [41] for meson-nucleon scatterings, using the results of a phase-shift analysis calculation using SAID [42], and modify them by fits to the data of the meson-nucleus elastic scatterings [43].

TABLE II. Input parameters of the density distributions $\rho_{p,n}(r)$ in the meson-nucleus optical potentials for π^- and K^+. All values are in fm.

Target	Density	$\langle r^2\rangle^{1/2}_{\rm ch}$	R_p	R_n	a
^{12}C	HO	2.44	1.552	1.552	1.333
^{28}Si	2pF	3.10	2.930	2.930	0.569
^{58}Ni	2pF	3.78	4.084	4.067	0.558
^{115}In	2pF	4.59	5.279	5.452	0.451
^{209}Bi	2pF	5.51	6.783	6.822	0.388

Considering the nuclear (π^-, K^+) reactions at the incident laboratory momentum $p_{\rm lab} = 1.2$ GeV/c, we use the distorted waves of π^- at $p_{\rm lab} = 1.2$ GeV/c and those of K^+ at $p_{\rm lab} \simeq 850$–600 MeV/c for $\omega \simeq 230$–430 MeV that corresponds to $-B_\Sigma \simeq (-50)$–$(+150)$ MeV. Thus we compute the angular distributions of the differential cross sections for these elastic scatterings in program PIRK [40], taking sufficiently the angular momenta with $\ell_{a,b} \lesssim 70$ for their partial waves due to large momentum transfer $q \simeq 400$–530 MeV/c in the (π^-, K^+) reactions. In Table II, we list the parameters of the density distribution $\rho_{p,n}(r)$ for various targets in these calculations.

1. π^--nucleus elastic scatterings

Figures 3 shows the calculated angular distributions for the π^- elastic scatterings on ^{12}C at $p_{\rm lab} = 800$ and 995 MeV/c, as a function of $\theta_{\rm c.m.}$, in comparison with those of the experimental data [43,44]. We find that the calculated angular distributions reproduce the data very well. For the incident laboratory momentum at 1.2 GeV/c for the nuclear (π^-, K^+) reactions, in which the parameters b_0 and c_0 are unknown due to the absence of the π^- elastic scattering data, we determine the values of b_0 and c_0 at $p_{\rm lab} = 1.2$ GeV/c, applying the same method to the standard Kisslinger potentials. Figure 4 displays the potential parameters $b_{0,1}$ and $c_{0,1}$ for π^- in the standard Kisslinger form, as a function of the incident laboratory momentum $p_{\rm lab}$. These parameters are used for various targets in this work.

2. K^+-nucleus elastic scatterings

Figure 5 shows the calculated angular distributions for the K^+ elastic scatterings on ^{12}C at $p_{\rm lab} = 715$ and 800 MeV/c. It has been known [45–47] that the K^+ scattering data are not well reproduced by the $t\rho$-type potential using a Fermi-averaged K^+N amplitude $b_0^{(KN)}$ based on the results from SAID [42]. We confirm that the calculated angular distributions are obviously underestimated in comparison with the data. In this work, we use the isoscalar parameters b_0 and c_0 that are determined by fitting to the data of the K^+ elastic scatterings on ^{12}C at $p_{\rm lab} = 635$, 715, and 800 MeV/c [43,48] in the

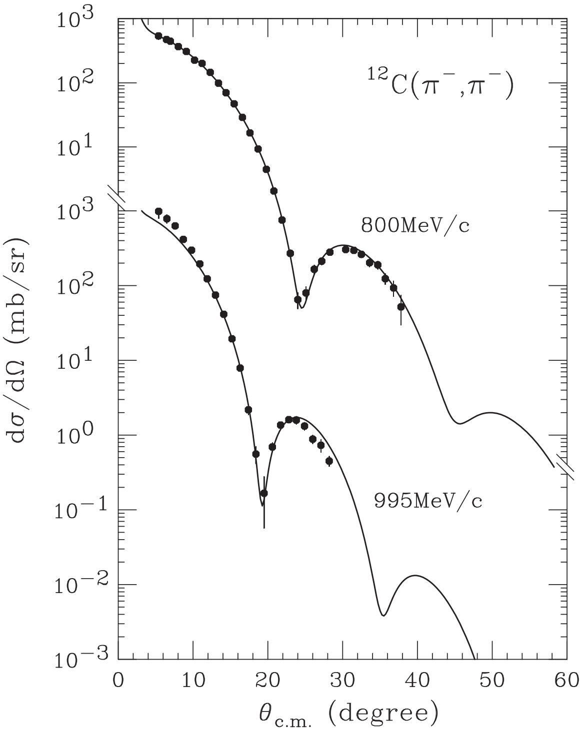

FIG. 3. Calculated angular distributions of differential cross sections for π^- elastic scatterings on the ^{12}C target at the incident laboratory momenta $p_{\rm lab} = 800$ and 995 MeV/c, as a function of the c.m. scattering angle $\theta_{\rm c.m.}$. The data are taken from Refs. [43,44].

standard Kisslinger form, as given in Fig. 6. The calculated angular distributions using these parameters agree with the data at $p_{\rm lab} = 715$ and 800 MeV/c very well, as seen in Fig. 5. Here the isovector parameters b_1 and c_1 for K^+ are assumed to be the same as $b_1^{(KN)}$ and $c_1^{(KN)}$ that are obtained by the Fermi-averaged K^+N amplitude. Therefore, one expects that

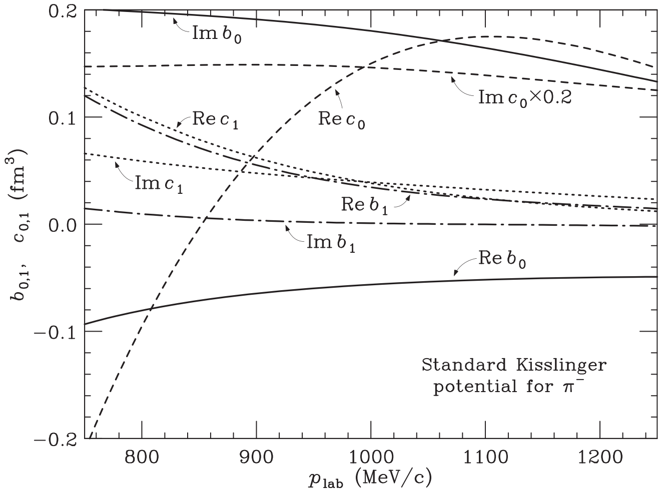

FIG. 4. The π^--nucleus optical potential parameters $b_{0,1}$ and $c_{0,1}$ in the standard Kisslinger form by using the Fermi-averaged π^-N amplitudes based on results from SAID [42], as a function of the incident laboratory momentum $p_{\rm lab}$.

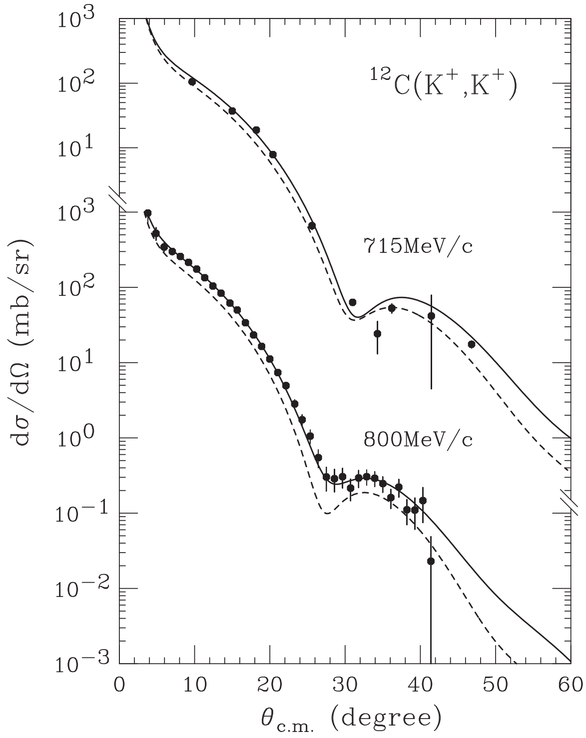

FIG. 5. Calculated angular distributions of differential cross sections for K^+ elastic scatterings on the ^{12}C target at the incident laboratory momenta $p_{\rm lab} = 715$ and 800 MeV/c, as a function of the c.m. scattering angle $\theta_{\rm c.m.}$. The solid curves are obtained by the standard Kisslinger form with the parameters b_0 and c_0 determined by fitting to the data. The dashed curves are obtained by the $t\rho$-type potential using a Fermi-averaged K^+N amplitude $b_0^{(KN)}$. The data are taken from Refs. [43,48].

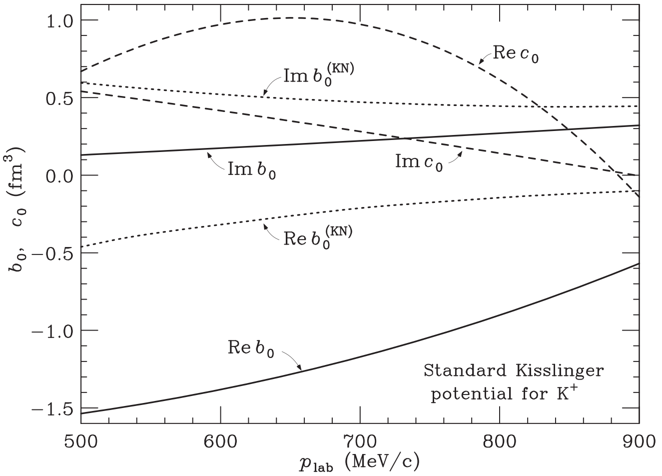

FIG. 6. The K^+-nucleus optical potential parameters b_0 and c_0 in the standard Kisslinger form by fits to the data of the K^+ elastic scatterings on ^{12}C [43,48], as a function of the incident laboratory momentum $p_{\rm lab}$. Solid and dashed curves denote the values of b_0 and c_0, respectively. Dotted curves denote the parameters $b_0^{(KN)}$ in the $t\rho$-type potential using a Fermi-averaged K^+N amplitude based on results from SAID [42].

the calculated spectra for the nuclear (π^-, K^+) reactions are improved theoretically by the use of the full distorted waves for π^- and K^+.

E. Σ-nucleus potentials

The Σ-nucleus (optical) potential is written as

$$U_\Sigma(E, r) = V_\Sigma(E, r) + iW_\Sigma(E, r), \tag{30}$$

where V_Σ and $W_\Sigma = W_\mathrm{e} + W_\mathrm{c}$ are the real and imaginary parts, respectively; W_e and W_c denote the absorptions arising from the nuclear excitation via $\Sigma N \to \Sigma N$ elastic scattering processes and $\Sigma N \to \Lambda N$ conversion ones, respectively. In previous papers [13,14], we discussed several types of the Σ-nucleus potential obtained by fitting to strong-interaction shifts and widths of the Σ^- atomic x-ray data [49–51]. Here we consider following potentials in a phenomenological way, which can sufficiently reproduce the experimental shifts and widths of the Σ^- atomic states: (a) the density-dependent (DD) potential [16] determined by fitting its phenomenological parameters (type A′) to the Σ^- atomic data; (b) the folding potential in the local density approximation (LDA) [36,52] with the YNG-NF interaction [53] based on the Nijmegen model F [54] by fits to the Σ^- atomic data, with modification of an odd-term strength in the real part and assuming $W_\mathrm{c}(r) = t\rho_p(r)$ in the imaginary part, where $\rho_p(r)$ is the proton density distribution and t is an effective strength parameter for fits to the data [19]; (c) the "$t_\mathrm{eff}\rho$" potential [16,18] determined earlier by an attractive effective ΣN scattering length $a = 0.36 + i0.20$ fm within a $t\rho$ form, fitting to the Σ^- atomic data for the light nuclei. In this section, we consider the Σ-nucleus potentials for the Σ^- atomic states and the Σ continuum states.

1. *Strong-interaction shifts and widths of Σ^- atomic states*

Because the Σ^- atomic (bound) states may have only the conversion decay, the imaginary potential is estimated by fits to the Σ^- atomic data, leading to the expression at $E < 0$ MeV. Thus we have the real and imaginary parts of the Σ-nucleus potential U_Σ at $E < 0$ MeV,

$$V_\Sigma(E, r) = V_\Sigma(r), \quad W_\Sigma(E, r) = W_\mathrm{c}(r). \tag{31}$$

In Figs. 7 and 8, we display the real and imaginary parts of the potentials for ^{27}Al and ^{208}Pb at $E \simeq 0$ MeV, as a function of the radial distance between a Σ^- hyperon and the center of the nucleus, using the potentials for (a) DD-A′, (b) LDA-NF, and (c) $t_\mathrm{eff}\rho$. Several Σ-nucleus potentials for light-to-heavy nuclei were also shown in Refs. [55,56].

To evaluate strong-interaction shifts and widths of Σ^- atomic (nl) states, we obtain complex eigenvalues, solving the Schrödinger equation with the Σ-nucleus potential U_Σ:

$$\left[-\frac{1}{2\mu}\nabla^2 + U_\Sigma(r) + U_\mathrm{Coul}(r)\right]\varphi_{nl}(r) = \left(E_{nl} - i\frac{\Gamma_{nl}}{2}\right)\varphi_{nl}(r), \tag{32}$$

where μ is the Σ^- nucleus reduced mass, and U_Coul is the Coulomb potential due to the finite charge distribution of the nucleus. The strong-interaction shifts are defined by $\varepsilon_{nl} = E_{nl}^{\mathrm{e.m.}} - E_{nl}$, where $E_{nl}^{\mathrm{e.m.}}$ are the electromagnetic energies including the nucleon size correction, the vacuum polarization to order $\alpha(Z\alpha)$ in the Coulomb potential.

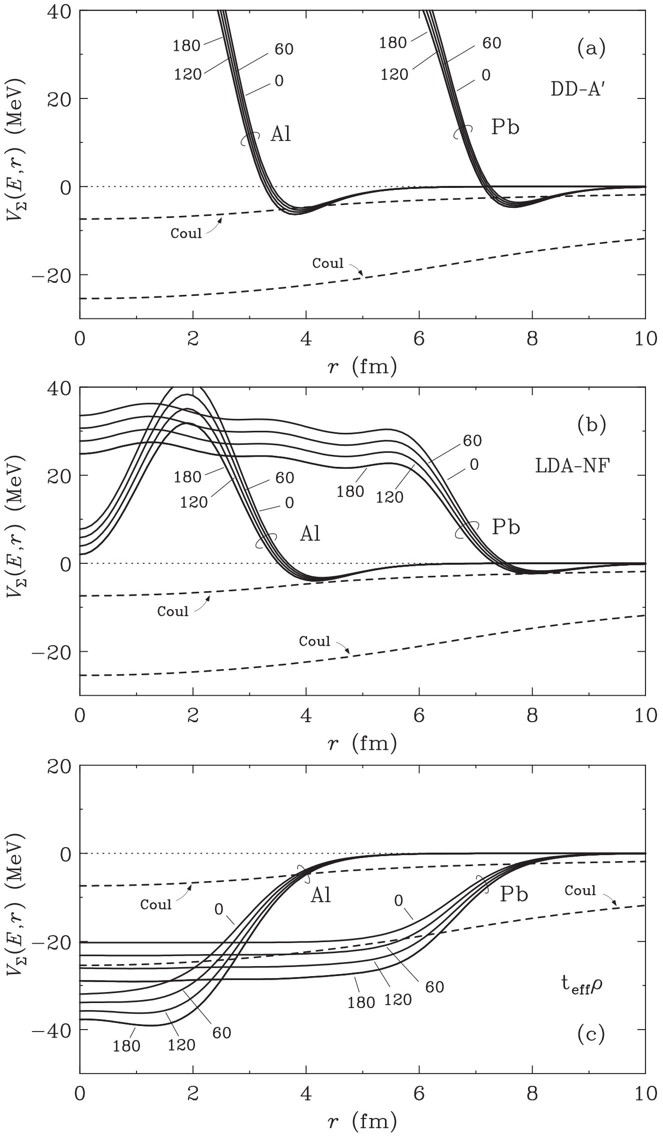

FIG. 7. Real parts $V_\Sigma(E, r)$ of the Σ-nucleus potentials for ^{27}Al and ^{208}Pb, as a function of the radial distance between a Σ^- hyperon and the center of the nucleus, calculated for (a) DD-A′, (b) LDA-NF, and (c) $t_\mathrm{eff}\rho$. Solid curves denote the energy dependences of the radial distributions of the potentials at $E = 0$, 60, 120, and 180 MeV, considering $V_\Sigma(E = 0, r) = V_\Sigma(r)$. Dashed curves denote the Coulomb potentials for ^{27}Al and ^{208}Pb.

In Table III, we list the calculated shifts and widths of the Σ^- atomic states, of which the available data ($N = 23$) are taken from C to Pb [49–51]. We find the χ^2 per degree of freedom $\chi^2/N = 20.06/23$ for DD-A′, 14.84/23 for LDA-NF, and 23.17/23 for $t_\mathrm{eff}\rho$. For the 17 data [49,50] omitting W and Pb, as discussed in Ref. [16], we find $\chi^2/N = 12.78/17$ for DD-A′, 10.74/17 for LDA-NF, and 10.82/17 for $t_\mathrm{eff}\rho$. These results are consistent with those analyzed by Refs. [16,57,58]. Our analysis indicates that these potentials explain the

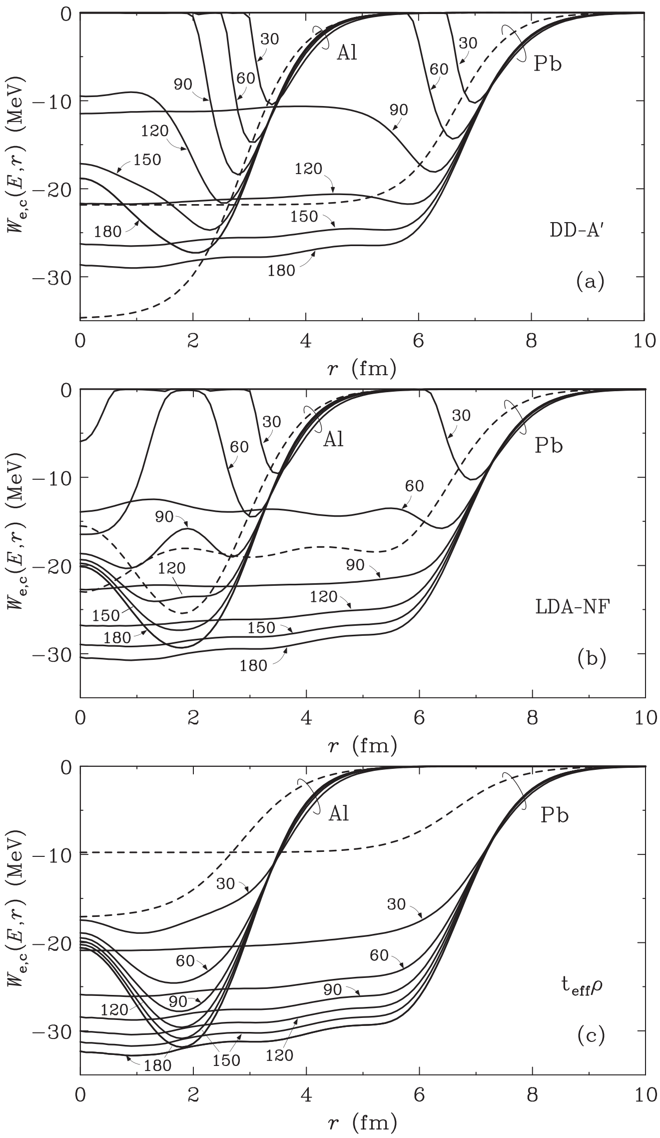

FIG. 8. Imaginary parts $W_\Sigma(E, r)$ of the Σ-nucleus potentials for ^{27}Al and ^{208}Pb, as a function of the radial distance between a Σ^- hyperon and the center of the nucleus. Solid curves denote the energy dependence of the radial distributions of the $W_{\rm e}(E, r)$ arising from the nuclear excitation via $\Sigma N \to \Sigma N$ elastic scattering processes at E = 30, 60, 90, 120, 150, and 180 MeV, for (a) DD-A′, (b) LDA-NF, and (c) $t_{\rm eff}\rho$. Dashed curves denote the radial distributions of $W_{\rm c}(E, r) = W_{\rm c}(r)$ arising from $\Sigma N \to \Lambda N$ conversion ones.

available data of the strong-interaction shifts and widths of the Σ^- atomic states because the values of the shifts and widths for Σ^- atomic states are mainly sensitive to the tail part of the indispensable attractive pocket outside the nuclear surface [16]; especially, the LDA-NF potential seems to be in very good agreement with the data of the shifts and widths including W and Pb [51] due to balance of the long-range repulsive and attractive components in V_Σ. Therefore, we confirm that all of the potentials enable us to sufficiently reproduce the experimental shifts and widths of the Σ^- atomic states, regardless of the different geometries among their potentials.

2. *Energy dependence of the potentials in Σ continuum states*

For Σ continuum states at the incident Σ-hyperon energy $E > 0$ MeV, we consider the energy dependence of the real part (V_Σ) of the potential in nuclear matter, introducing an effective mass μ^* [59] in Eq. (11):

$$E = \frac{\boldsymbol{p}^2}{2\mu} + V_\Sigma(E, \rho)$$
$$\simeq \frac{\boldsymbol{p}^2}{2\mu^*} + V_\Sigma(E = 0, \rho), \tag{33}$$

where

$$\frac{\mu^*}{\mu} = 1 - \frac{d}{dE} V_\Sigma(E, \rho) \equiv \nu'_\Sigma. \tag{34}$$

Here we assume the density dependence of ν'_Σ in the form [19]

$$1/\nu'_\Sigma = 1 + (1/\nu'_{\Sigma 0} - 1)\rho/\rho_0, \tag{35}$$

where $\nu'_{\Sigma 0} = 1.05$ is chosen practically, as we will discuss based on the semimicroscopic LDA-NF in Sec. IV D. Note that the quantity ν'_Σ is a function of the radial distance through the nuclear density distribution $\rho(r)$ for finite nuclei. Therefore, substituting Eq. (34) into Eq. (33) and rearranging the equation, one can easily derive the real part of the energy-dependent potential for $E > 0$ MeV, which is defined by

$$V_\Sigma(E, r) = V_\Sigma^{(0)}(r) + V_\Sigma^{(1)}(r)E, \tag{36}$$

with

$$V_\Sigma^{(0)}(r) \equiv V_\Sigma(r), \quad V_\Sigma^{(1)}(r) \equiv 1 - \nu'_\Sigma(r), \tag{37}$$

where $V_\Sigma(r)$ is the real potential determined for the Σ^- atomic states in Sec. II E 1, which should be regarded as $\nu'_\Sigma V_\Sigma(E = 0, \rho)$. Because the energy dependence of phenomenological potentials such as DD-A′ and $t_{\rm eff}\rho$ is theoretically unknowable, we assume the same energy dependence as in Eq. (34) estimated by LDA-NF for these types of the Σ-nucleus potentials. In Fig. 7, we display the energy dependence of $V_\Sigma(E, r)$ for ^{27}Al and ^{208}Pb at E = 0, 60, 120, and 180 MeV, using the Σ-nucleus potentials for DD-A′, LDA-NF, and $t_{\rm eff}\rho$.

For the imaginary parts (W_Σ) of the potentials, we obtain $W_{\rm e}$ and $W_{\rm c}$ in a semiclassical estimation, as shown in the Appendix. We realize that the absorption $W_{\rm e}$ arising from the nuclear excitation via the $\Sigma N \to \Sigma N$ scatterings is dominant as E increases, in contrast to the $\Sigma^- p \to \Lambda n$ conversion decays in which $W_{\rm c}$ does not depend much on E [60], i.e., $W_{\rm c}(E, r) \simeq W_{\rm c}(r)$, so we assume the same $W_{\rm c}$ determined phenomenologically by fits to the Σ^- atomic data for simplicity. Indeed, g-matrix calculations [61] indicate that the strength of $W_{\rm c}$ is not very dependent on E, whereas $W_{\rm e}$ has a remarkable energy dependence. Therefore, the imaginary potentials at $E > 0$ MeV are written as

$$W_\Sigma(E, r) \simeq W_{\rm e}(E, r) + W_{\rm c}(r). \tag{38}$$

In Fig. 8, we also show the energy dependence of the calculated absorption potentials $W_{\rm e}(E, r)$ for ^{27}Al and ^{208}Pb at E = 30, 60, 90, 120, 150, and 180 MeV, using the Σ-nucleus potentials for DD-A′, LDA-NF, and $t_{\rm eff}\rho$. Here we used the same $\nu'_{\Sigma 0} = 1.05$ for these potentials. We find that the radial distribution of $W_{\rm e}(E, r)$ for DD-A′ (LDA-NF) behaves as a

TABLE III. Calculated strong-interaction shifts and widths of Σ^- atomic (nl) states for the $n+1 \to n$ transitions, in comparison with the available data of the Σ^- x-ray measurements [49–51]. All energies and widths are in eV. The values of χ^2/N are obtained by comparing the calculated shifts and widths with these data.

Transition		DD-A$'$			LDA-NF			$t_{\rm eff}\rho$			Expt.		
	$n+1 \to n$	ε	Γ	$\Gamma_{\rm u}$	ε	Γ	$\Gamma_{\rm u}$	ε	Γ	$\Gamma_{\rm u}$	ε	Γ	$\Gamma_{\rm u}$
C	$4 \to 3$	7.19	26.7	0.012	28.1	31.1	0.014	21.3	41.8	0.012			0.031 ± 0.012
O	$4 \to 3$	36.6	318.3	0.40	301.7	453.9	0.49	252.0	768.3	0.42	320 ± 230		1.0 ± 0.7
Mg	$5 \to 4$	30.6	49.3	0.079	45.6	45.3	0.071	30.5	52.3	0.070	25 ± 40	<70	0.11 ± 0.09
Al	$5 \to 4$	74.8	110.4	0.21	80.3	84.4	0.15	62.4	112.1	0.18	68 ± 28	43 ± 75	0.24 ± 0.06
Si	$5 \to 4$	135.3	228.4	0.52	155.3	178.7	0.37	123.9	254.9	0.45	159 ± 36	220 ± 110	0.41 ± 0.10
S	$5 \to 4$	427.9	871.3	2.91	550.2	766.3	2.46	418.8	1171.8	2.53	360 ± 220	870 ± 700	1.5 ± 0.8
Ca	$6 \to 5$	29.9	41.2	0.13	43.4	38.0	0.12	26.0	42.2	0.12			0.41 ± 0.22
Ti	$6 \to 5$	101.2	144.9	0.61	119.2	117.7	0.48	87.8	155.1	0.52			0.65 ± 0.42
Ba	$9 \to 8$	38.3	84.1	1.02	45.7	33.3	0.38	34.2	49.1	0.49			2.9 ± 3.5
W	$10 \to 9$	90.5	99.1	1.75	102.7	83.6	1.61	77.2	118.0	1.67	214 ± 60	18 ± 149	2 ± 2
Pb	$10 \to 9$	440.7	524.1	12.5	388.2	394.2	16.7	381.0	707.5	11.8	422 ± 56	428 ± 158	17 ± 3
	χ^2/N		20.06/23			14.78/23			23.17/23				
			12.78/17			10.69/17			10.82/17				

surface-peaked form at low energies of $E \lesssim 90$ (60) MeV, and turns to a volume form at high energies of $E \gtrsim 120$ (90) MeV, as shown in Figs. 8(a) and 8(b). This behavior is because V_Σ has a repulsion inside the nuclear surface and an attraction outside the nucleus, and $U_{\rm Coul}$ is an attractive Coulomb potential. For $t_{\rm eff}\rho$, we confirm that the radial distribution of $W_{\rm e}(E, r)$ is in a normal volume form, as shown in Fig. 8(c), because V_Σ is purely attractive.

To study the repulsion and absorption of the potential, we also use the energy-independent potentials with the WS form with $R = 1.1(A-1)^{1/3}$ fm and $a = 0.67$ fm in Eq. (1), which reproduce the QF spectra in previous works [13,14,22]: (d) the WS form with the strengths of $V_0^\Sigma = +20$ MeV and $W_0^\Sigma = -20$ MeV (type A); (e) the WS form with the strengths of $V_0^\Sigma = +30$ MeV and $W_0^\Sigma = -40$ MeV (type B). These strengths of the WS-B potential are also consistent with those for Σ^--^{5}He [22], which were recently obtained by the analysis of the ^{6}Li(π^-, K^+) reaction in the J-PARC E10 experiment [23]. However, we stress that any WS potential with a repulsive tail cannot reproduce attractive strong-interaction shifts of the Σ^- atomic data due to its repulsion.

III. RESULTS

Saha *et al.* [3] have experimentally measured the data of the (π^-, K^+) reactions on ^{12}C, ^{28}Si, ^{58}Ni, ^{115}In, and ^{209}Bi targets in the KEK-E438 experiment. The average cross sections $\bar{\sigma}_{4^\circ\text{–}8^\circ}$ were obtained by the K^+ scattering angles of 6° ± 2° in the laboratory frame:

$$\bar{\sigma}_{4^\circ\text{-}8^\circ} \equiv \int_{\theta_{\rm lab}=4^\circ}^{\theta_{\rm lab}=8^\circ} \left(\frac{d^2\sigma}{dE_K d\Omega_K}\right) d\Omega \Bigg/ \int_{\theta_{\rm lab}=4^\circ}^{\theta_{\rm lab}=8^\circ} d\Omega. \tag{39}$$

To compare with the data, here we calculate the inclusive spectra of these (π^-, K^+) reactions at $p_{\rm lab} = 1.2$ GeV/c and $\theta_{\rm lab} = 6^\circ$, taking into account a detector resolution [3]. We use several types of the Σ-nucleus potentials for ^{11}B, ^{27}Al, ^{57}Co, ^{114}Cd, and ^{208}Pb, for which the final states are produced by the (π^-, K^+) reactions on ^{12}C, ^{28}Si, ^{58}Ni, ^{115}In, and ^{209}Bi targets, respectively, as mentioned in Sec. II E. For the amplitude of $\overline{f}_{\pi^- p \to K^+\Sigma^-}$ for each target, we take into account the binding effects in the nucleus. Thus we compare the calculated spectrum for each target with the 56–65 data points in the QF region including from the Σ^- bound to the Σ^- continuum states, introducing a renormalization factor f_s into its absolute value to make a fit to the spectral shape of the data for the whole spectrum because the value of $\overline{f}_{\pi^- p \to K^+\Sigma^-}$ would still have some ambiguities [13,14,22]. Because the spectrum in the Σ^- near-threshold region is very sensitive to the Σ-nucleus potential [31], we also study the shape behavior of the calculated spectrum, introducing another renormalization factor f_s focusing on the 21 data points in the near-threshold region. We examine the sensitivity of the spectrum to the nature of the Σ-nucleus potentials for DD-A$'$, LDA-NF, $t_{\rm eff}\rho$, WS-A, and WS-B in the (π^-, K^+) reactions on the light-to-heavy nuclei, as mentioned below.

A. ^{28}Si target

In Fig. 9, we show the calculated spectra on ^{28}Si in the QF region ($\omega = 220$–441 MeV) and the near-threshold region ($\omega = 220$–302 MeV), taking into account a detector resolution of 3.5 MeV FWHM [3]. Here we consider the calculated spectra for DD-A$'$, LDA-NF, and $t_{\rm eff}\rho$, taking the single-particle energies of proton hole states for $(1s_{1/2})^{-1}$, $(0d_{5/2})^{-1}$, $(0p_{1/2})^{-1}$, $(0p_{3/2})^{-1}$, and $(0s_{1/2})^{-1}$ orbits in ^{28}Si, as listed in Table I, with configurations obtained by density-dependent Hartree-Fock calculations [36,37]. We find that the calculated spectra for DD-A$'$ and LDA-NF are in good agreement with the data, i.e., $\chi^2/N \simeq 0.7$–0.8 with $f_s \simeq 1.0$–1.1 for the QF and near-threshold regions, as shown in Table IV. Therefore, the magnitudes of the calculated cross sections are significantly improved ($f_s \simeq 1$) by the KG distorted waves for the QF and near-threshold regions [13], in comparison with

TABLE IV. The χ^2 fitting for various Σ-nucleus potentials in the (π^-, K^+) reactions on ^{12}C, ^{28}Si, ^{58}Ni, ^{115}In, and ^{209}Bi targets at $p_{\text{lab}} = 1.2$ GeV/c and $\theta_{\text{lab}} = 6^\circ$. The values of χ^2/N and the renormalized factor f_s are obtained by comparing the calculated spectrum with the N data points for the near-threshold and QF regions [3].

	DD-A′		LDA-NF		$t_{\text{eff}}\rho$		WS-A		WS-B		d.o.f.
Target	χ^2/N	f_s	χ^2/N	f_s	χ^2/N	f_s	χ^2/N	f_s	χ^2/N	f_s	N
Near-threshold region											
^{12}C	1.008	1.129	1.074	1.210	1.057	0.648	0.689	1.344	0.484	1.102	21
^{28}Si	0.822	1.041	0.813	1.111	1.109	0.628	0.284	1.369	0.259	1.066	21
^{58}Ni	1.163	1.140	1.273	1.089	1.859	0.603	0.683	1.576	0.434	1.156	21
^{115}In	0.780	1.011	0.828	0.933	1.029	0.497	0.587	1.092	0.541	0.885	21
^{209}Bi	0.627	1.028	0.662	0.990	0.770	0.578	0.478	1.145	0.234	0.970	21
QF region											
^{12}C	1.201	1.080	1.198	1.082	1.963	0.791	0.942	1.154	0.942	1.206	54
^{28}Si	0.813	1.015	0.767	1.022	2.736	0.807	0.724	1.075	0.423	1.156	65
^{58}Ni	0.938	0.982	0.957	0.930	1.390	0.696	1.945	1.023	0.847	1.074	56
^{115}In	0.647	0.946	0.737	0.879	1.734	0.649	0.623	0.895	0.513	0.948	57
^{209}Bi	0.557	1.044	0.599	1.013	1.445	0.751	0.428	1.045	0.366	1.075	52

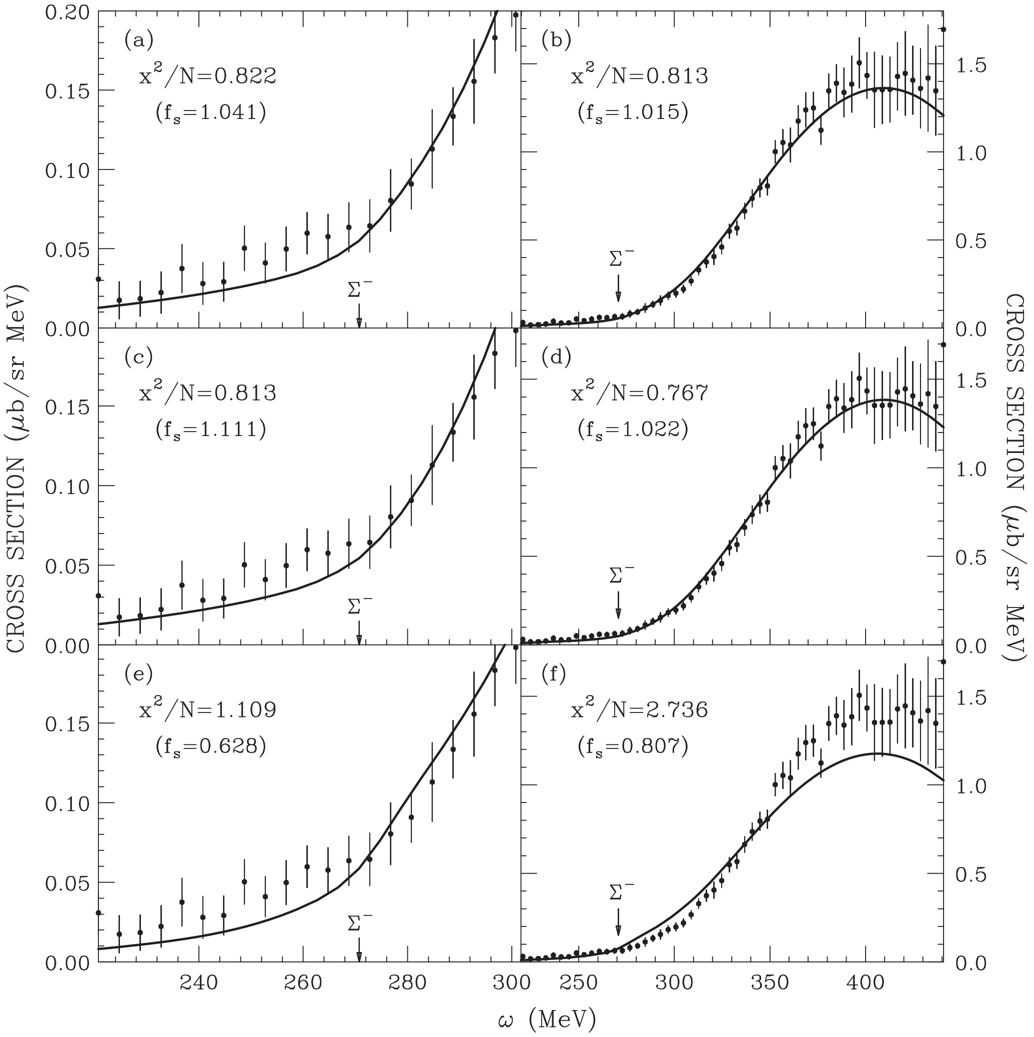

FIG. 9. Calculated spectra of the ^{28}Si(π^-, K^+) reaction at $p_{\text{lab}} = 1.2$ GeV/c (6°) in the near-threshold region [(a), (c), (e)] and in the QF region [(b), (d), (f)], together with the data from the KEK-E438 experiment [3]. The solid curves denote the spectra with the potentials for [(a), (b)] DD-A′, [(c), (d)] LDA-NF, and [(e), (f)] $t_{\text{eff}}\rho$, where the calculated spectrum is normalized by each factor f_s. The spectra are folded with a detector resolution of 3.5 MeV FWHM.

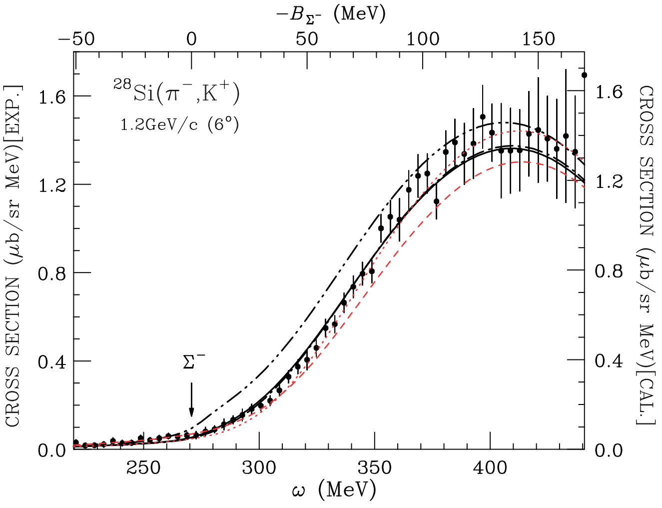

FIG. 10. Calculated spectra of the $^{28}\mathrm{Si}(\pi^-, K^+)$ reaction at $p_{\mathrm{lab}} = 1.2$ GeV/c (6°) in the QF region, together with the data [3]. Solid, dot-dashed, and dot-dot-dashed curves denote the spectra with the potentials for DD-A′, LDA-NF, and $t_{\mathrm{eff}}\rho$, respectively. Dotted and dashed curves also denote the potentials for WS-A and WS-B, respectively. All of the calculated spectra are normalized by $f_s = 1.015$ obtained for DD-A′. These spectra are folded with a detector resolution of 3.5 MeV FWHM.

$f_s \simeq 0.5$ by the eikonal ones in the previous work [13]. We realize that the calculated spectra for DD-A′ and LDA-NF fully explain the shape and magnitude of the data in the $^{28}\mathrm{Si}(\pi^-, K^+)$ reactions, and their spectra are very similar to each other regardless of the different geometry among the potentials. On the other hand, the calculated spectrum for $t_{\mathrm{eff}}\rho$ cannot reproduce the data satisfactorily, requiring $\chi^2/N \simeq 2.7$ with $f_s \simeq 0.81$ in the QF region, although a relatively good $\chi^2/N \simeq 1.1$ with $f_s \simeq 0.63$ in the near-threshold region. The purely attractive potential such as $t_{\mathrm{eff}}\rho$ cannot explain the (π^-, K^+) data, leading to the rejection of the potential.

One may expect that the shapes and magnitudes of the calculated cross sections mainly depend on the strength of the absorptions of the Σ-nucleus potentials and their repulsion. To see the sensitivity of the spectra to the Σ-nucleus potentials, we compare their absolute cross sections in the QF region. Figure 10 displays the calculated spectra for DD-A′, LDA-NF, $t_{\mathrm{eff}}\rho$, WS-A, and WS-B in the $^{28}\mathrm{Si}(\pi^-, K^+)$ reaction, together with the data [3]; all of the spectra are normalized by a factor of $f_s = 1.015$ obtained for DD-A′. We find that the nature of the potentials discriminates the shapes and magnitudes of the spectra in the QF region. However, the differences among these spectra are not so large. The magnitude of the spectrum for attractive $t_{\mathrm{eff}}\rho$ is larger than those for DD-A′ and LDA-NF [13]. The magnitude of the spectrum for repulsive WS-A having the energy-independent $(V_0^\Sigma, W_0^\Sigma) = (+20\,\mathrm{MeV}, -20\ \mathrm{MeV})$ with $R = 1.1(A-1)^{1/3}$ fm and $a = 0.67$ fm is as large as those for them at $\omega \simeq 350$ MeV, but the slope of its shape is too steep. The magnitude of the spectrum for more repulsive WS-B having $(V_0^\Sigma, W_0^\Sigma) = (+30\,\mathrm{MeV}, -40\ \mathrm{MeV})$ is moderately smaller than those for DD-A′, LDA-NF, and WS-A, whereas it instead reproduces the data in the near-threshold region very well.

Note that the peak positions of these spectra are located at $\omega \simeq 400$ MeV, which are slightly shifted downward energetically, compared to $\omega \simeq 420$ MeV in the previous work [14]. These shifts originate from the energy dependence of $(d\sigma/d\Omega)^{\mathrm{opt}}$ due to the binding effects of the proton hole states in the OFA.

B. ^{209}Bi target

In Fig. 11, we show the calculated spectra for DD-A′, LDA-NF, and $t_{\mathrm{eff}}\rho$ on a heavier target, ^{209}Bi, taking into account a detector resolution of 5.2 MeV FWHM [3]. We compare them with the data [3] in the QF region ($\omega = 212$–433 MeV) and the near-threshold region ($\omega = 213$–294 MeV). Here we assume the configuration of $[^{208}\mathrm{Pb} \otimes 0h_{9/2}]$ with $J^P = 9/2^-$ for the ^{209}Bi target, considering single-particle wave functions for 16 hole states, as listed in Table I. We find that the calculated spectra for DD-A′ and LDA-NF reproduce the data by taking $\chi^2/N \simeq 0.6$ with $f_s \simeq 1.0$ in the QF region and $\chi^2/N \simeq 0.6$–0.7 with $f_s \simeq 1.0$ in the near-threshold region, as seen in Table IV. The calculated spectrum for $t_{\mathrm{eff}}\rho$ does not make a good fit to the data in the QF region, by taking a relatively small value of $f_s \simeq 0.75$.

Figure 12 displays the calculated spectra for DD-A′, LDA-NF, $t_{\mathrm{eff}}\rho$, WS-A, and WS-B in the $^{209}\mathrm{Bi}(\pi^-, K^+)$ spectra, together with the data [3]; all of the spectra are normalized by a factor of $f_s = 1.044$ obtained for DD-A′. We find that the shapes and magnitudes of the spectra slightly differ. This result also indicates that the quantitative constraints on the Σ-nucleus potential for the spectrum on ^{209}Bi are not clearer than those on ^{28}Si, as pointed out in Ref. [14].

One may expect to extract the isovector contribution in the Σ-nucleus potential for ^{208}Pb in which the real and imaginary parts of the isovector components are given by

$$U_1^\Sigma \langle \Sigma^- \text{-}^{208}\mathrm{Pb} | \boldsymbol{T}_C \cdot \boldsymbol{t}_\Sigma | \Sigma^- \text{-}^{208}\mathrm{Pb} \rangle / A_{\mathrm{core}}, \tag{40}$$

where U_1^Σ is an isovector term of the Σ-nucleus potential. This matrix element of Eq. (40) contributes to that of the Σ-nucleus potentials by about 10%, as discussed in Ref. [14]. Therefore, we cannot determine the isovector components of U_Σ meaningfully, analyzing the $^{209}\mathrm{Bi}(\pi^-, K^+)$ data. When we use the common strengths for the WS-B potential having $(V_0^\Sigma, W_0^\Sigma) = (+30\,\mathrm{MeV}, -40\ \mathrm{MeV})$ without the isovector term, we realize that the calculated spectrum can simulate the $^{209}\mathrm{Bi}(\pi^-, K^+)$ data very well, as seen in Table IV.

C. χ^2 fittings for light-to-heavy nuclei

Figure 13 displays the calculated spectra for various potentials in the (π^-, K^+) spectra on ^{12}C, ^{58}Ni, and ^{115}In targets, compared to the data [3]; all of the spectra are normalized by a factor of f_s that is obtained for DD-A′ by fits to the data for each target; i.e., $f_s = 1.080$ for ^{12}C, $f_s = 0.982$ for ^{58}Ni, and $f_s = 0.946$ for ^{115}In. We find that the calculated spectra on these targets can explain the data of the KEK-E438 experiment quantitatively, as well as those on ^{28}Si and ^{209}Bi targets.

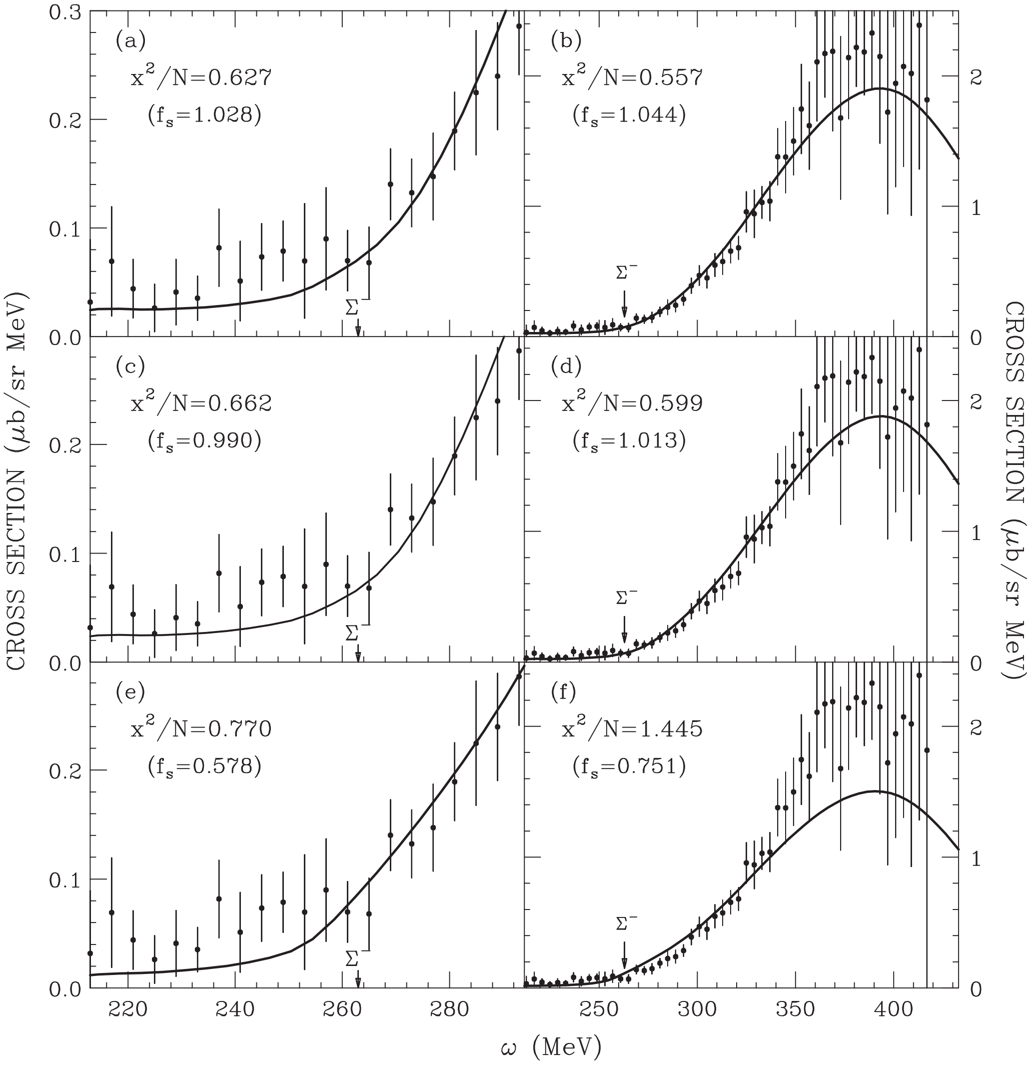

FIG. 11. Calculated spectra of the ^{209}Bi(π^-, K^+) reaction at $p_{\rm lab} = 1.2$ GeV/c (6°) in the near-threshold region [(a), (c), (e)] and in the QF region [(b), (d), (f)], together with the data from the KEK-E438 experiment [3]. The spectra are folded with a detector resolution of 5.2 MeV FWHM. See the caption in Fig. 9.

In Table IV, we list the calculated results of the χ^2 per degree of freedom (d.o.f.), χ^2/N, and the renormalization factor f_s required by fits to the data on light-to-heavy nuclei, ^{12}C, ^{28}Si, ^{58}Ni, ^{115}In, and ^{209}Bi, in order to examine the properties of the Σ-nucleus potentials for DD-A′, LDA-NF, $t_{\rm eff}\rho$, WS-A, and WS-B. In Table V, we show the total values of the χ^2 per degree of freedom, $\chi^2_{\rm tot}/N_{\rm tot}$, where $\chi^2_{\rm tot} = \sum \chi^2$ for all data points of $N_{\rm tot} = 54 + 65 + 56 + 57 + 52 = 284$ for the QF region and $N_{\rm tot} = 21 \times 5 = 105$ for the near-threshold region. We find $\chi^2_{\rm tot}/N_{\rm tot} = 0.831$ (0.880), 0.850 (0.930), 1.886 (1.165), 0.932 (0.544), and 0.613 (0.390) for DD-A′, LDA-NF, $t_{\rm eff}\rho$, WS-A, and WS-B in the QF (near-threshold) region, respectively. These results confirm that the potentials having a repulsion inside the nuclear surface and an attraction outside the nucleus with a sizable absorption [13,14] reproduce sufficiently the data of the (π^-, K^+) reaction on the light-to-heavy nuclei because $\chi^2_{\rm tot}/N_{\rm tot} \lesssim 1$ for DD-A′ and LDA-NF. The calculated spectra for WS-B are also in excellent agreement with the data ($\chi^2_{\rm tot}/N_{\rm tot} = 0.613$ for the QF region) in terms of the fits to the (π^-, K^+) spectra, as shown in Table V. The absolute value of the spectrum for WS-B becomes more similar to those for DD-A′ and LDA-NF when it is used for a larger nucleus such as ^{208}Bi, as seen in Figs. 10, 12, and 13.

Consequently, we recognize that the spectra with the potentials for DD-A′ and LDA-NF provide the ability to reproduce the data from C to Pb; the Σ-nucleus potentials having a repulsion inside the nuclear surface and an attractive pocket outside the nucleus with a sizable absorption can explain the data of the Σ^- atoms and the (π^-, K^+) spectra simultaneously, regardless of the different strengths and ranges of these potentials. When we adopted the KG distorted waves for π^- and K^+ and the absorption including $W_{\rm e}(E)$, we therefore updated and improved the shape and magnitude of the calculated spectra in the nuclear (π^-, K^+) reaction within the DWIA.

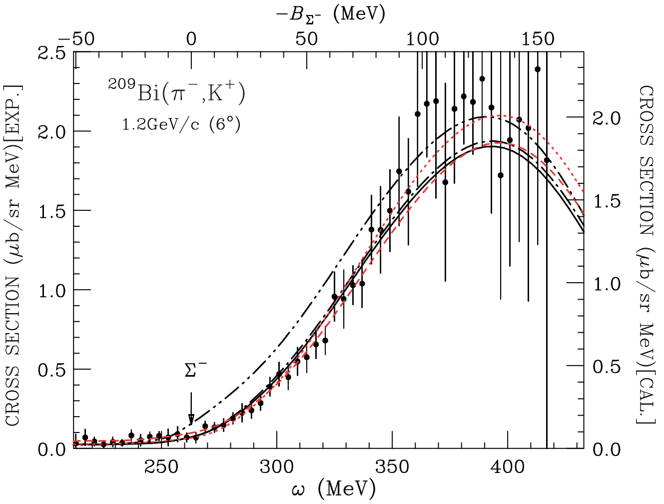

FIG. 12. Calculated spectra of the ^{209}Bi(π^-, K^+) reaction at $p_{\rm lab} = 1.2$ GeV/c (6°) in the QF region, together with the data [3]. The value of $f_s = 1.044$ obtained for DD-A′ is used. These spectra are folded with a detector resolution of 5.2 MeV FWHM. See the caption of Fig. 10.

IV. DISCUSSION

A. Mass number dependence of the integrated cross sections

In Sec. III, we show that our KG distorted waves for π^- and K^+ give a successful description for explaining the spectra on (π^-, K^+) reactions on various targets from C up to Bi. To clearly see a mass-number dependence of the Σ^- production on the nuclear (π^-, K^+) reaction, we consider the integrated cross sections $\sigma(^A{\rm Z})$ on the target ^{A}Z, which is given by integrating over the spectrum for $-22 < E < 82$ MeV as

$$\sigma(^A{\rm Z}) \equiv \int_{-22\ {\rm MeV}}^{82\,{\rm MeV}} \left(\frac{d^2\sigma}{dE_K d\Omega_K} \right) dE. \qquad (41)$$

In Table VI, we show the calculated results of the integrated cross sections $\sigma(^A{\rm Z})$ at $p_{\rm lab} = 1.2$ GeV/c and $\theta_{\rm lab} = 6°$, together with the data obtained from Ref. [3], using the potentials for DD-A′, LDA-NF, $t_{\rm eff}\rho$, WS-A, and WS-B. Figure 14 shows the mass-number A dependence of the integrated cross sections $\sigma(^A{\rm Z})$ for these potentials. The data for $\sigma(^A{\rm Z})$ are roughly evaluated as a function of $C \times A^\alpha$, where C is a constant and $\alpha = 0.161 \pm 0.018$, whose value is slightly smaller than $\alpha = 0.20 \pm 0.04$ that was suggested by the ratio of the inclusive spectrum for each target to that for Si [3]. We confirm that, although the magnitudes of $\sigma(^{12}{\rm C})$ [$\sigma(^{115}{\rm In})$] are slightly smaller [larger] than the data, the magnitudes of $\sigma(^A{\rm Z})$ are almost consistent with those of the data; the tendency of the A dependence of $\sigma(^A{\rm Z})$ agrees with that of the data in the use of the KG distorted waves, whereas the degree to which the data matches depends on the type of the Σ-nucleus potential. We have $\alpha = 0.189, 0.207, 0.201, 0.235,$ and 0.236 for DD-A′, LDA-NF, $t_{\rm eff}\rho$, WS-A, and WS-B, respectively. This difference may originate from the balancing between a repulsion and an absorption in these potentials including the isovector components.

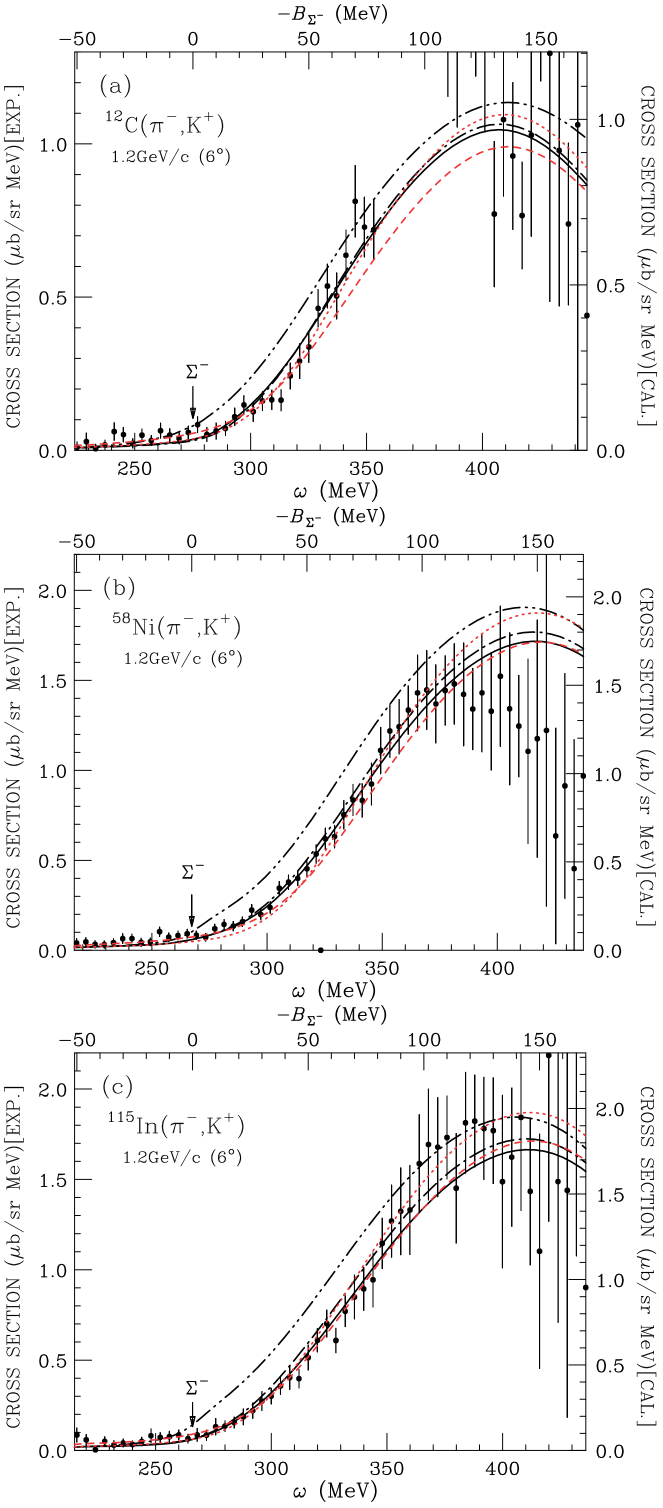

FIG. 13. Calculated spectra of the (π^-, K^+) reactions on (a) ^{12}C, (b) ^{58}Ni, and (c) ^{115}In at $p_{\rm lab} = 1.2$ GeV/c (6°) in the QF region, together with the data [3]. See the caption in Fig. 10.

To clearly see the effects of the KG distorted waves for π^- and K^+ on the spectra, we compare them with those obtained in the eikonal approximation having $\sigma_\pi = 38$ mb and $\sigma_K = 18$ mb, and $\alpha_\pi = \alpha_K = 0$. Such eikonal parameters

TABLE V. The χ^2 fitting for the Σ-nucleus potentials in the (π^-, K^+) reactions on ^{12}C, ^{28}Si, ^{58}Ni, ^{115}In, and ^{209}Bi targets at $p_{\rm lab} = 1.2$ GeV/c and $\theta_{\rm lab} = 6^\circ$. The values of $\chi^2_{\rm tot}/N_{\rm tot}$ are estimated by $\chi^2_{\rm tot} = \sum \chi^2$ for all data points of $N_{\rm tot} = 21 \times 5 = 105$ for the near-threshold region and $N_{\rm tot} = 54 + 65 + 56 + 57 + 52 = 284$ for the QF region.

	$\chi^2_{\rm tot}/N_{\rm tot}$	
Target	Near-threshold region	QF region
DD-A′	0.880	0.831
LDA-NF	0.930	0.850
$t_{\rm eff}\rho$	1.165	1.886
WS-A	0.544	0.932
WS-B	0.390	0.613

were determined to reproduce the data of the Λ production cross sections for ${}^{12}_{\Lambda}$C in the (π^+, K^+) reactions at $p_{\rm lab} = 1.05$ and 1.2 GeV/c [15]. Their eikonal distortions seem to be consistent with those reported by Ref. [62], in which the distortion factors are equal to $C_{\rm dist} = 0.4$–0.2 from C up to Y targets, in the Λ productions via the nuclear (π^+, K^+) reactions using $\sigma_\pi = 34$ mb and $\sigma_K = 15$ mb.

In Fig. 1, we have shown the A dependences of $\sigma({}^A{\rm Z})$ for the potentials for DD-A′ and WS-B in the eikonal calculations, together with the values of the data. To compare with the data, we must artificially reduce the absolute values of $\sigma({}^A{\rm Z})$ by a scaling factor of 0.5, in which the slopes of their $\sigma({}^A{\rm Z})$ are almost similar to those in other eikonal estimations [3], as a function of A. We find that the slopes of $\sigma({}^A{\rm Z})$ using the eikonal approximation are larger than those using KG, comparing between the results shown in Figs. 1 and 14; we have $\alpha = 0.309$ for the former and $\alpha = 0.189$ for the latter when we use the DD-A′ potential. Therefore, we show that the KG distorted waves improve significantly the A dependence of the cross sections in the DWIA, as well as the magnitude of the spectra, as already discussed in Sec. III C.

B. Implication from the effective number of protons

TABLE VI. Comparison of the calculated values of the integrated cross section $\sigma({}^A{\rm Z})$ with the data of the (π^-, K^+) reactions on ^{12}C, ^{28}Si, ^{58}Ni, ^{115}In, and ^{209}Bi at $p_{\rm lab} = 1.2$ GeV/c and $\theta_{\rm lab} = 6^\circ$. The data are estimated from Ref. [3].

Target	Present calc. $\sigma({}^A{\rm Z})$ (μb/sr)					Expt. [3]
^{A}Z	DD-A′	LDA-NF	$t_{\rm eff}\rho$	WS-A	WS-B	(μb/sr)
^{12}C	25.38	25.35	33.89	23.62	22.45	26.84 ± 4.62
^{28}Si	32.67	32.15	43.03	28.79	27.84	30.04 ± 2.87
^{58}Ni	35.85	38.00	51.67	32.52	32.30	34.09 ± 4.36
^{115}In	41.42	44.85	61.09	43.20	41.24	36.21 ± 5.72
^{209}Bi	45.16	46.52	60.87	44.82	43.47	43.88 ± 7.78
χ^2/N	0.39	0.77	12.55	0.46	0.49	
α	0.189	0.207	0.201	0.235	0.236	0.161 ± 0.018

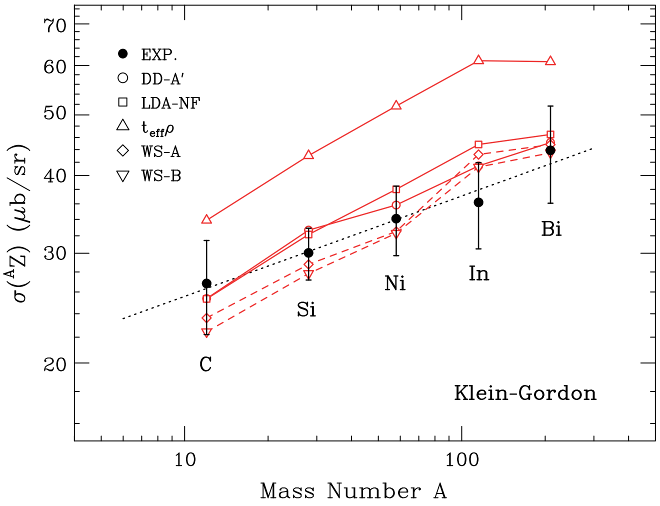

FIG. 14. Mass-number dependence of the integrated cross sections $\sigma({}^A{\rm Z})$ from C up to Bi targets at $p_{\rm lab} = 1.2$ GeV/c and $\theta_{\rm lab} = 6^\circ$, in the DWIA with the KG distorted waves. Various potentials are used. The dotted line denotes $A^{0.161}$ for fits to the data as an eye guide. The data are estimated from Ref. [3].

When the production probabilities via the DWIA framework are considered, it is useful to deal with the effective number of protons [26,63–65]. The total effective number of protons $Z^{\rm tot}_{\rm eff}$ is written as

$$Z^{\rm tot}_{\rm eff} = \int_0^\infty Z_{\rm eff}(r)dr, \tag{42a}$$

$$Z_{\rm eff}(r) = \int r^2 \rho_p(r) D_{\pi K}(\boldsymbol{r}) d\Omega, \tag{42b}$$

$$D_{\pi K}(\boldsymbol{r}) = \frac{1}{4\pi}\left|\chi^{(-)*}_{\boldsymbol{p}_K}(\boldsymbol{r})\chi^{(+)}_{\boldsymbol{p}_\pi}(\boldsymbol{r})\right|^2, \tag{42c}$$

where $\rho_p(r)$ denotes a radial distribution of a proton density normalized by $\int \rho_p(r) d\boldsymbol{r} = Z$, and $D_{\pi K}(r)$ is the meson absorption factor caused by the distorted waves for π^- and K^+.

Figure 15 displays the calculated radial distributions of $Z_{\rm eff}(r)$ in the (π^-, K^+) reactions at $p_{\rm lab} = 1.2$ GeV/c on ^{12}C, ^{28}Si, ^{58}Ni, ^{115}In, and ^{209}Bi targets, as a function of the radial distance between the proton and the center of the target nucleus. Here the factors $D_{\pi K}(r)$ for $E = 0$ MeV were used. We find that the magnitudes of the distributions $Z_{\rm eff}(r)$ for the KG distorted waves are almost half as large as those of the eikonal ones. Their radial shapes become smaller toward the interior of the nucleus due to the absorption factor $D_{\pi K}(r)$ as A increases. This fact leads to the cross sections $\sigma({}^A{\rm Z})$ for KG being smaller by a factor of 2–4 than those with the eikonal distorted waves, as seen in Fig. 14. We realize that the A dependence of $\sigma({}^A{\rm Z})$ is influenced on the behavior of $Z_{\rm eff}(r)$.

In Table VII, we show the calculated effective numbers of protons $Z^{\rm tot}_{\rm eff}$ in the (π^-, K^+) reactions at $p_{\rm lab} = 1.2$ GeV/c on these targets, comparing the KG and eikonal distortions. We find $Z^{\rm tot}_{\rm eff}/Z \simeq 0.2$ (0.4) for ^{28}Si and $Z^{\rm tot}_{\rm eff}/Z \simeq 0.05$ (0.13) for ^{209}Bi in the KG (eikonal) estimations. This behavior originates from a stronger absorption for the KG distorted waves in heavier nuclei, leading to $Z^{\rm tot}_{\rm eff} \simeq 3.9$–$4.3$.

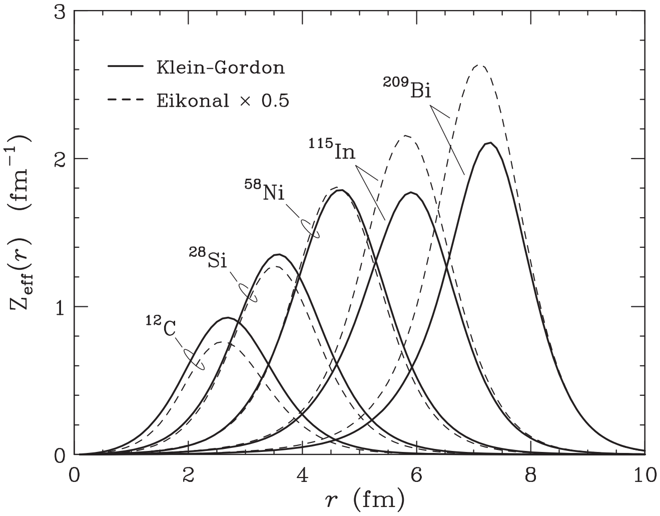

FIG. 15. Calculated effective number of protons $Z_{\rm eff}(r)$ in the (π^-, K^+) reactions at $p_{\rm lab} = 1.2$ GeV/c on ^{12}C, ^{28}Si, ^{58}Ni, ^{115}In, and ^{209}Bi targets, as a function of the radial distance between the proton and the center of the target nucleus. Solid curves denote the values of $Z_{\rm eff}(r)$ using the KG distorted waves. Dashed curves are obtained by using the eikonal distorted waves, which are scaled by a factor of 0.5.

C. Effective volume integrals of the Σ-nucleus potentials

As seen in Figs. 7 and 8, although the radial distributions of DD-A′ in nuclei are different from those of LDA-NF, we show that calculated spectra for DD-A′ are very similar to those for LDA-NF. In Ref. [14], we argued the reasons why the calculated spectra cannot distinguish the radial distributions of the potentials for DD-A′ and LDA-NF, introducing the *effective* volume integral per nucleon of the Σ-nucleus potential, which may be given by

$$J_R^{\rm eff} + iJ_I^{\rm eff} = \frac{1}{A_{\rm eff}^{\rm tot}} \int_0^\infty A_{\rm eff}(r) U_\Sigma(r) dr, \tag{43a}$$

$$A_{\rm eff}^{\rm tot} = \int_0^\infty A_{\rm eff}(r) dr, \tag{43b}$$

$$A_{\rm eff}(r) = Z_{\rm eff}(r) + N_{\rm eff}(r), \tag{43c}$$

where $A_{\rm eff}^{\rm tot}$ is the total effective number of nucleons with the radial distributions of $Z_{\rm eff}(r)$ and $N_{\rm eff}(r)$ for protons and neutrons. In Table VIII, we show the real ($J_R^{\rm eff}$) and imaginary ($J_I^{\rm eff}$) parts of the effective volume integrals per nucleon for the potentials at $E = 60$ MeV, using the KG distorted waves. These values are expected to effectively represent the nature of the potentials with the meson distortions in the (π^-, K^+) reactions on nuclei. In the case of DD-A′, we find $(J_R^{\rm eff}, J_I^{\rm eff}) = (-17.14$ MeV fm^3, -63.68 MeV fm$^3)$ for Σ^--^{27}Al and $(-2.960$ MeV fm^3, -17.84 MeV fm$^3)$ for Σ^--^{208}Pb, values that are almost the same as those of LDA-NF. This result means that the calculated spectra of the nuclear (π^-, K^+) reactions cannot distinguish the radial distributions of these potentials due to the meson distortions that give us limited information concerning their radial distribution near the nuclear surface.

TABLE VII. Calculated effective number of protons $Z_{\rm eff}^{\rm tot}$ in the (π^-, K^+) reactions at $p_{\rm lab} = 1.2$ GeV/c on several targets with a number of protons Z.

		Klein-Gordon		Eikonal	
Target	Z	$Z_{\rm eff}^{\rm tot}$	$Z_{\rm eff}^{\rm tot}/Z$	$Z_{\rm eff}^{\rm tot}$	$Z_{\rm eff}^{\rm tot}/Z$
C	6	1.87	0.312	2.94	0.490
Si	14	2.86	0.204	5.12	0.366
Ni	28	3.93	0.140	7.68	0.274
In	49	3.90	0.080	9.24	0.189
Bi	83	4.31	0.052	10.96	0.132

In Table VIII, on the other hand, we also show the real (J_R) and imaginary (J_I) parts of the volume integral per nucleon of the Σ-nucleus potentials, omitting the meson distortions by $D_{\pi K}(r) \to 1$ in Eq. (42b). Advantageous differences of (J_R, J_I) among these potentials are expected to identify the radial distribution of the Σ-nucleus potential by testing the angular distributions of elastic scattering from a Σ^- hyperon from nuclei. This approach is a standard way for examining the radial distribution of an optical potential in nuclear physics. Note that the angular distribution of the differential cross sections in the Σ^- elastic scattering from nuclei provides detailed information to discriminate the nature of the repulsion/attraction inside the nuclear surface in the Σ-nucleus potentials, as discussed in Ref. [56].

D. Validity of the real part of the Σ-nucleus potential

It is known that the real and imaginary parts of the nuclear optical potential are generally energy dependent, according to the standard lowest-order Brueckner (LOB) theory. Yamamoto *et al.* [61] have studied the Σ-nucleus systems in the LOB g-matrix calculations. Their work indicates that, although the strength of $W_{\rm e}$ in nuclear matter has a strong energy dependence for ESC08 potentials, the strength of $W_{\rm c}$ and also V_Σ are weakly energy dependent, depending on the kind of the effective ΣN interaction quantitatively. Because the effective ΣN interactions are still ambiguous at the present stage, the Σ-nucleus potentials determined by phenomenological ways [13,14,22] may be advantageous over those by microscopic ones. In this paper, therefore, we have assumed that the energy dependence of the real part V_Σ of the Σ-nucleus potential in the Σ continuum states ($E > 0$ MeV) is given by the effective mass $\mu^* = \nu'_\Sigma \mu$, and the real and imaginary parts of the potentials at $E = 0$ MeV are equal to those of the potentials obtained phenomenologically by fitting the data of the Σ^- atomic states. Thus we estimate the energy dependence of $U_\Sigma(E, r)$ as shown in Figs. 7 and 8.

To check the validity of this assumption for V_Σ in our calculations, we attempt to evaluate the energy dependence of V_Σ for the LDA-NF potential, which is constructed by the folding potential procedure [61] with a modified YNG-NF interaction [53]. Figure 16 displays the calculated strengths of V_Σ for LDA-NF in ^{208}Pb at the center, as a function of E, together with the calculated values of V_Σ obtained by ESC08a [61] and of V_N for a nucleon in the ordinary nuclei [59] using the LOB g-matrix calculations at $k_F = 1.35$ fm^{-1}. We find that

TABLE VIII. Real and imaginary parts of the effective volume integrals per nucleon ($J_R^{\rm eff}$, $J_I^{\rm eff}$) and the volume integrals per nucleon (J_R, J_I) in the Σ-nucleus potentials for Σ^--^{27}Al and Σ^--^{208}Pb at $E = 60$ MeV. All values are in unit of MeV fm^3.

	Σ^--^{27}Al				Σ^--^{208}Pb			
Potentials	$J_R^{\rm eff}$	$J_I^{\rm eff}$	J_R	J_I	$J_R^{\rm eff}$	$J_I^{\rm eff}$	J_R	J_I
DD-A′	−17.14	−63.11	159.8	−260.9	−2.960	−17.84	319.3	−193.4
LDA-NF	−16.56	−60.04	88.69	−247.5	−2.219	−17.66	152.0	−242.3
$t_{\rm eff}\rho$	−37.41	−54.92	−177.4	−254.0	−8.677	−15.96	−144.5	−236.3
WS-A	47.80	−47.80	156.9	−156.9	9.210	−9.210	123.1	−123.1
WS-B	71.70	−95.61	235.4	−313.8	13.81	−18.42	184.7	−246.3

the energy dependence of V_Σ for LDA-NF is relatively weak in comparison with that of V_N. The value of the derivative dV_Σ/dE at $\rho = \rho_0$ is estimated in a linear approximation by

$$\frac{dV_\Sigma}{dE}\bigg|_{\rho=\rho_0} \simeq \frac{24-33}{170-0} \simeq -0.05 = 1 - \nu'_{\Sigma 0}, \qquad (44)$$

as shown in Fig. 16. Thus we confirm that the value of $\nu'_{\Sigma 0} = 1.05$ for the effective mass μ^* in Eq. (33) is acceptable in our calculations, which leads to less effect on the nuclear (π^-, K^+) spectra determined by the behavior of the potential U_Σ near the nuclear surface, as seen in Table VIII.

On the other hand, microscopic calculations for the Σ-nucleus potentials based on the modern YN and YNN interactions may be needed to understand the properties of the potential U_Σ and to clarify their interactions themselves quantitatively. This investigation would be one of the most critical subjects in subsequent studies.

E. Effects of the absorptions arising from the nuclear excitation via $\Sigma N \to \Sigma N$ scatterings

To see the effects of the absorptions $W_{\rm e}$ on the spectra, we demonstrate the calculated spectra for DD-A′, omitting $W_{\rm e}$ in the imaginary part of the Σ-nucleus potentials: For Σ^--^{27}Al, we have $\chi^2/N \simeq 0.68$ with $f_s \simeq 1.01$ in the QF region and $\chi^2/N \simeq 0.54$ with $f_s \simeq 1.22$ in the near-threshold region. For Σ^--^{208}Pb, we have $\chi^2/N \simeq 0.53$ with $f_s \simeq 1.08$ in the QF region and $\chi^2/N \simeq 0.61$ with $f_s \simeq 1.26$ in the near-threshold region. These results indicate that the normalization factor f_s in the near-threshold region is about 25% larger than that of the QF one, and suggests that only $W_\Sigma(E=0,r) = W_{\rm c}(r)$ is insufficient to explain the data for both regions simultaneously. We also find that the calculated spectra including the energy dependence of $W_{\rm e}$ are obviously favored, as seen in Figs. 10 and 12. This argument for DD-A′ is very similar to that for LDA-NF. Therefore, we recognize that the energy dependence of $W_{\rm e}$ plays an important role in reproducing the data; the absolute values of the calculated cross sections are in very good agreement with those of the data in the near-threshold and QF regions simultaneously.

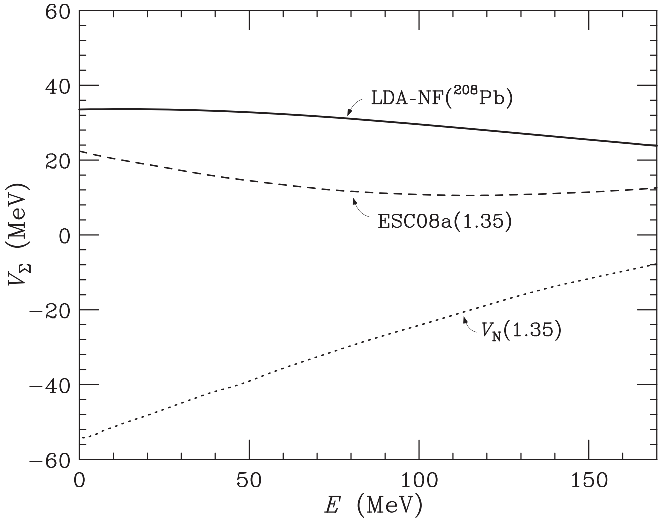

FIG. 16. Calculated strengths of V_Σ for LDA-NF in ^{208}Pb at the center, as a function of E, together with the calculated values of V_Σ for ESC08a [61] and of V_N for the nucleon [59] in the LOB g-matrix calculations at $k_F = 1.35$ fm^{-1}.

The finite range corrections of the real and imaginary parts of the nuclear optical potentials in the LDA are often evaluated using the improved LDA (ILDA) [59]. In the ILDA, the imaginary part of the potentials $\overline{W}_{\rm e}(E,r)$, as given in Eq. (A8b), is replaced by

$$\overline{W}_{\rm e}(E,r) = (b\sqrt{\pi})^{-3}\int W^{\rm (e)}_{\rm NM}(k_\Sigma(r'),\rho(r')) \times \exp(-|\boldsymbol{r}-\boldsymbol{r}'|^2/b^2)d\boldsymbol{r}', \qquad (45)$$

where b denotes a range parameter. When the density-dependent effective interaction has a zero range, the quantity $\overline{W}_{\rm e}(E,r)$ is equivalent to that in the LDA. Thus our semiclassical estimation for $\overline{W}_{\rm e}(E,r)$ is exactly this case. Therefore, the LDA treatment may be compatible with the $\langle v\sigma\rangle\rho$ form obtained by total cross sections and zero-range interaction in the semiclassical estimation.

For example, in the case of LDA-NF for Σ^--^{208}Pb, we take the range of $b = 1.0$ fm and consider the finite range effects on the imaginary part $W_{\rm e}$. On the other hand, the real part for the LDA-NF (folding) potential already contains the finite range effects [52] because of the density-dependent YNG-NF [53]. We find that the calculated spectrum in the ILDA is visually indistinguishable from that in the LDA, whereas the QF value of $\chi^2/N = 0.613$ in the former is slightly worse than that of $\chi^2/N = 0.599$ for the latter due to the stretched potential distribution near the nuclear surface. The effective volume integrals may reveal why the calculated spectrum has little influence on this correction in $W_{\rm e}$, as seen in Table VIII; using $J_I^{\rm eff} = -20.34$ (-17.66) MeV fm^3 for the ILDA (LDA) at $E = 60$ MeV, we estimate the relative difference to the

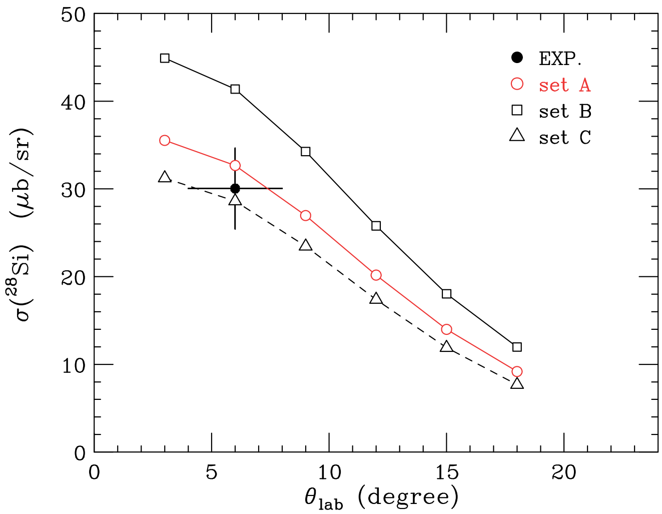

FIG. 17. Angular dependence of the integrated cross sections $\sigma(^{28}\mathrm{Si})$ for DD-A′ at $p_{\rm lab} = 1.2$ GeV$/c$ and $\theta_{\rm lab} = 3^\circ, 6^\circ, 9^\circ, 12^\circ, 15^\circ$, and 18°. The parameter sets for A, B, and C are used for the optical potential for K^+. See the text.

volume integral,

$$\Delta = \left|\frac{J_I^{\rm eff}(\mathrm{ILDA}) - J_I^{\rm eff}(\mathrm{LDA})}{J_I}\right| = \frac{2.68}{242.3} \simeq 0.011, \quad (46)$$

so that we have the small value of $\Delta \simeq 1\%$ due to the meson distortions. Consequently, we show that the imaginary parts of the potentials in the LDA are acceptable, as well as those in the ILDA.

F. Sensitivity to optical potentials for mesons

When we analyze the data of the nuclear (π^-, K^+) reactions within the DWIA quantitatively, we will need precise wave functions for the distorted waves of π^- and K^+, as well as those of the nucleon and Σ^- hyperon in the nucleus. Thus it may mean naively that the nuclear (π^-, K^+) spectra provide valuable information on the radial behavior of the partial waves for the distorted waves for π^- and K^+ to investigate the properties of these optical potentials inside the nucleus.

To see the sensitivity of the spectra to the K^+-nucleus optical potential, here, we estimate the integrated cross sections $\sigma(^{28}\mathrm{Si})$ for DD-A′ at $p_{\rm lab} = 1.2$ GeV$/c$. Because of the mysterious K^+ behavior in nuclear medium [45–47], the parameters for K^+ remain to be determined in a standard Kisslinger or $t\rho$-type potential. We consider the following three different parameters: b_0 and c_0 obtained by fits to the data of the K^+ elastic scatterings on ^{12}C in this work (set A); $b_0 = -6.2 \times 10^{-4} p_K + i\,90/p_K$ (fm^3) that well reproduces the same data [25] (set B); $b_0^{(KN)}$ obtained by the Fermi-averaged K^+N amplitudes based on the results from SAID [42], as seen in Fig. 6 (set C).

Figure 17 shows the angular dependence of the integrated cross sections $\sigma(^{28}\mathrm{Si})$ at $\theta_{\rm lab} = 3^\circ, 6^\circ, 9^\circ, 12^\circ, 15^\circ$, and 18°. We find that the calculated results of the integrated cross sections for sets A and C are consistent with the data of 30.04 ± 2.87 μb/sr at $\theta_{\rm lab} = 6^\circ$, though the latter does not well reproduce the data of the K^+ elastic scatterings on ^{12}C. Despite the parameters for set B also being obtained by fits to the K^+ elastic scatterings on ^{12}C, their integrated cross sections are about 30% larger than those for set A. This discrepancy may be due to the different behavior of the distorted waves inside the nucleus.

Note that the A dependence in the nuclear (π^-, K^+) reactions rather depends on uncertain neutron density distributions $\rho_n(r)$ by which the optical potentials for π^- and K^+ are constructed for the KG distorted waves, together with proton density distributions $\rho_p(r)$. Because the π^- and K^+ mesons are strongly absorbed in the neutron skin in heavy nuclei, the production cross sections in the nuclear (π^-, K^+) reaction are sensitive to the choice of the neutron radius R_n in the optical potentials listed in Table II, together with the parameters $b_{0,1}$ and $c_{0,1}$ in Eq. (28). Thus we realize that the nuclear (π^-, K^+) spectra provide the ability of examining the radial behavior of the distorted waves for π^- and K^+ inside the nucleus. More detailed studies of the KG distorted waves for $\pi^\mp$ and K^+ in hypernuclear $(\pi^\mp, K^+)$ productions are needed for the future subjects.

V. SUMMARY AND CONCLUSION

We have studied theoretically the Σ^- production in the (π^-, K^+) reaction on ^{12}C, ^{28}Si, ^{58}Ni, ^{115}In, and ^{209}Bi targets in the framework of the DWIA with the OFA for the elementary $\pi^- p \to K^+\Sigma^-$ t matrix. We have used the Σ-nucleus potentials that are determined by fits to the Σ^- atomic x-ray data and that take into account the energy dependence arising from the nuclear excitation via the $\Sigma N \to \Sigma N$ scatterings with the Σ hyperon effective mass. We have examined the calculated spectra, adopting the distorted waves obtained by solving the KG equation for π^- and K^+. Thus we have compared these spectra with those of the nuclear (π^-, K^+) data at the KEK-E438 experiment. The results are summarized as follows:

(1) The KG distorted waves for π^- and K^+ fully improve the magnitudes of the calculated spectra for the Σ^- production cross sections in the DWIA for explaining the nuclear (π^-, K^+) data at the KEK-E438 experiment.
(2) The Σ-nucleus potentials with DD-A′ and LDA-NF provide the ability to reproduce the data of the (π^-, K^+) reactions on ^{12}C, ^{28}Si, ^{58}Ni, ^{115}In, and ^{209}Bi, whereas it is still difficult to determine the radial distribution of the Σ-nucleus potential inside the nucleus and its strength at the center.
(3) The A dependence of the integrated cross sections agrees with that of the data from light to heavy targets in the DWIA with the KG distorted waves, depending on the properties of the Σ-nucleus potential. This result is also sensitive to the parameters $b_{0,1}$ and $c_{0,1}$ in the Kisslinger potentials for π^- and K^+ where a neutron density distribution is unknown in heavier nuclei.
(4) The optimal Fermi-averaged t matrix for $\pi^- p \to K^+\Sigma^-$ reactions including the binding effects of the

struck protons plays an important role in describing the shapes of the measured (π^-, K^+) spectra.

In conclusion, we can explain quantitatively the data of the (π^-, K^+) reactions on nuclear targets at the KEK-E438 experiment. The full distorted waves for π^- and K^+ provide a good description of the shapes and magnitudes of the Σ^- production spectra in the DWIA analysis using the OFA for the $\pi^- p \to K^+\Sigma^-$ reaction. The resultant calculated spectra are in excellent agreement with the data. We confirm that the potentials having a repulsion inside the nuclear surface and an attraction outside the nucleus with a sizable absorption reproduce sufficiently the data of the Σ^- atomic x-ray and the (π^-, K^+) reactions on the light-to-heavy targets, regardless of the different geometries among their potentials. Such nuclear (π^-, K^+) reactions may be among the most promising tools for studying wave functions for K^+ inside a nucleus in order to settle the long-standing problem of K^+ in the nuclear medium [47]. More microscopic calculations for the Σ-nucleus potentials based on the modern YN potentials are also needed for understanding YN and YNN interactions. These investigations are subjects for future research.

ACKNOWLEDGMENTS

The authors thank Prof. A. Gal and Prof. E. Oset for valuable comments in the early stage of this research. This work was supported by Grants-in-Aid for Scientific Research (KAKENHI) from the Japan Society for the Promotion of Science: Scientific Research (C) (Grant No. JP20K03954).

APPENDIX: SEMICLASSICAL ESTIMATION FOR W_Σ

The width of nuclear (or hypernuclear) resonant states can be decomposed into two parts [66]:

$$\Gamma = \Gamma^{\uparrow} + \Gamma^{\downarrow}, \tag{A1}$$

where the escape width $\Gamma^{\uparrow}$ describes the direct emission of a particle and a core nucleus into continuum states, and the spreading width $\Gamma^{\downarrow}$ describes the spread of doorway nuclear states into the surrounding nuclear excitation. The estimate of the spreading width in nuclear matter (NM) identifies the absorption as

$$W_{\mathrm{NM}} = -\tfrac{1}{2}\Gamma^{\downarrow}_{\mathrm{NM}}, \tag{A2}$$

which corresponds to the imaginary part of the optical potential. In the case of Σ-hypernuclear states [66], the spreading width is divided into two components,

$$\Gamma^{\downarrow}_{\Sigma} = \Gamma^{\downarrow}_{\mathrm{e}} + \Gamma^{\downarrow}_{\mathrm{c}}, \tag{A3}$$

where $\Gamma^{\downarrow}_{\mathrm{e}}$ expresses the results of the $\Sigma N \to \Sigma N$ interaction, and $\Gamma^{\downarrow}_{\mathrm{c}}$ expresses the results of the $\Sigma N \to \Lambda N$ conversion interaction. This conversion processes in nuclei induce the nuclear breakup dominantly even if a Σ hyperon is bound because the converted ΛN pair has a large energy from the mass difference of $\Delta M = m_\Sigma - m_\Lambda \simeq 80$ MeV. Gal and Dover [67] first discussed a semiclassical estimation for W_Σ with the $\Sigma N \to \Lambda N$ conversion cross section. The widths of the hypernuclear states are also discussed in terms of nuclear Auger transitions [68,69]. Thus, the imaginary part of the Σ-nucleus potential is written by

$$W_\Sigma(E, r) = W_{\mathrm{e}}(E, r) + W_{\mathrm{c}}(E, r), \tag{A4}$$

where W_{e} and W_{c} denote the absorptions arising from the nuclear excitation via $\Sigma N \to \Sigma N$ elastic scattering processes and $\Sigma N \to \Lambda N$ conversion ones, respectively.

According to Dąbrowski and Rożynek [19,60], we estimate the absorption potential $W_\Sigma(E, r)$ that has an E dependence in the Σ-nucleus scatterings. By applying the optical theorem to the lowest-order Brueckner (LOB) theory with the effective mass approximation [60], the absorption potentials W_{NM} at a nuclear density ρ and a Σ-hyperon momentum k_Σ in NM are written in a semiclassical approximation as

$$\begin{aligned} W^{(\mathrm{e})}_{\mathrm{NM}}(k_\Sigma, \rho) = -\tfrac{1}{4}\nu'_{\Sigma N}\rho\langle v_{\Sigma N} Q_\Sigma[&\sigma(\Sigma^- p \to \Sigma^0 n) \\ &+ \sigma(\Sigma^- p \to \Sigma^- p) + \sigma(\Sigma^- n \to \Sigma^- n)]\rangle, \end{aligned} \tag{A5}$$

$$W^{(\mathrm{c})}_{\mathrm{NM}}(k_\Sigma, \rho) = -\tfrac{1}{4}\nu'_{\Lambda N}\rho\langle v_{\Sigma N} Q_\Lambda \sigma(\Sigma^- p \to \Lambda n)\rangle, \tag{A6}$$

where $\langle\cdots\rangle$ denotes the average value in the Fermi sea, ν'_{YN} is a ratio of the effective to the real for the YN reduced masses, $v_{\Sigma N}$ is a ΣN relative velocity, and Q_Y is the Pauli exclusion operator. The nucleon effective mass denotes $m^*_N = \nu'_N m_N$, which is compatible with the empirical energy dependence of the nuclear optical potential [19,59]. For hyperon effective mass parameters, we use the density dependence of the form [19]

$$1/\nu'_Y = 1 + (1/\nu'_{Y0} - 1)\rho/\rho_0, \tag{A7}$$

where $\nu'_{\Sigma 0} = 1.05$ for the Σ hyperon and $\nu'_{\Lambda 0} = 0.70$ for the Λ hyperon, as discussed for the LOB g-matrix calculations [61]. The quantities $\sigma(\Sigma N \to \Sigma N)$ and $\sigma(\Sigma N \to \Lambda N)$ are the total cross sections for the $\Sigma N \to \Sigma N$ and $\Sigma N \to \Lambda N$ scattering processes, respectively. In a good approximation of σ in NM to σ in free space [60,70], we use the total cross sections for $\Sigma^- p \to \Sigma^- p$, $\Sigma^- p \to \Sigma^0 n$, $\Sigma^+ p \to \Sigma^+ p$, and $\Sigma^- p \to \Lambda n$ processes, simulating the results calculated by the ΣN next-to-leading order (NLO) potential in chiral EFT [71] up to 900 MeV/c instead of the experimental data that are still unknown at high energies. In the local density approximation (LDA), we obtain the absorption potentials for finite nuclei, which are written by

$$W_\lambda(E, r) = \left(\frac{\mu^*}{\mu}\right)\overline{W}_\lambda(E, r), \tag{A8a}$$

$$\overline{W}_\lambda(E, r) = W^{(\lambda)}_{\mathrm{NM}}(k_\Sigma(r), \rho(r)), \tag{A8b}$$

where $\lambda = \{\mathrm{e}, \mathrm{c}\}$. Here the local momentum $k_\Sigma(r)$ may be given by

$$k_\Sigma(r) \simeq \sqrt{2\mu\{E - V_\Sigma(E, r) - U_{\mathrm{Coul}}(r)\}}, \tag{A9}$$

where μ is the reduced mass between the Σ^- hyperon and the core nucleus, V_Σ is the real part of the Σ-nucleus potential in Eq. (36), and U_{Coul} is the Coulomb potential between the Σ^- hyperon and the nucleus. The expression of Eq. (A6) was applied for estimating the shifts and widths of the Σ^- atomic states ($E < 0$ MeV), as discussed in Ref. [19]. The quantities Q_Y and ν'_Y in W_e, which play an essential role at $\rho \simeq \rho_0$, can behave as $Q_Y \to 1$ and $\nu'_Y \to 1$ at the low density $\rho \to 0$, so that we have $W_\mathrm{e} \propto 4\pi\, \mathrm{Im}(f_{\Sigma N})\rho$ in LDA. This just corresponds to the potential using the density dependent effective interaction with the zero range, which may be compatible with the semiclassical estimation in Eqs. (A5) and (A6). Figure 8 displays the energy dependence of the radial distributions of $W_\mathrm{e}(E, r)$ arising from the nuclear excitation via $\Sigma N \to \Sigma N$ elastic scattering processes for Σ^--^{27}Al and Σ^--^{208}Pb. This semiclassical estimation seems to work well as an approximation as the LOB g-matrix calculations [61].

[1] A. Gal, E. V. Hungerford, and D. J. Millener, Rev. Mod. Phys. **88**, 035004 (2016).
[2] H. Noumi *et al.*, Phys. Rev. Lett. **89**, 072301 (2002); **90**, 049902(E) (2003).
[3] P. K. Saha *et al.*, Phys. Rev. C **70**, 044613 (2004).
[4] C. B. Dover, D. J. Millener, and A. Gal, Phys. Rep. **184**, 1 (1989), and references therein.
[5] T. Harada, Y. Akaishi, S. Shinmura, and H. Tanaka, Nucl. Phys. A **507**, 715 (1990).
[6] T. Harada, Phys. Rev. Lett. **81**, 5287 (1998); Nucl. Phys. A **672**, 181 (2000).
[7] M. Oka *et al.*, Phys. Lett. B **130**, 365 (1983).
[8] M. M. Nagels, Th. A. Rijken, and Y. Yamamoto, Phys. Rev. C **99**, 044003 (2019); Y. Fujiwara *et al.*, Prog. Part. Nucl. Phys. **58**, 439 (2007); J. Haidenbauer, U.-G. Meisner, and A. Nogga, Eur. Phys. J. A **56**, 91 (2020).
[9] S. R. Beane *et al.* (NPLQCD Collaboration), Phys. Rev. Lett. **106**, 162001 (2011); T. Inoue, N. Ishii, S. Aoki, T. Doi, T. Hatsuda, Y. Ikeda, K. Murano, H. Nemura, and K. Sasaki (HAL QCD Collaboration), *ibid.* **106**, 162002 (2011).
[10] T. Inoue (HAL QCD Collaboration), in *Proceedings of the 13th International Conference on Hypernuclear and Strange Particle Physics: HYP2018*, edited by L. Tang and R. Schumacher, AIP Conf. Proc. No. 2130 (AIP, New York, 2019), p. 020002.
[11] I. Vidaña, Proc. R. Soc. A **474**, 20180145 (2018).
[12] S. Balberg and A. Gal, Nucl. Phys. A **625**, 435 (1997); M. Baldo, G. F. Burgio, and H.-J. Schulze, Phys. Rev. C **58**, 3688 (1998), and references therein.
[13] T. Harada and Y. Hirabayashi, Nucl. Phys. A **759**, 143 (2005).
[14] T. Harada and Y. Hirabayashi, Nucl. Phys. A **767**, 206 (2006).
[15] T. Harada and Y. Hirabayashi, Nucl. Phys. A **744**, 323 (2004).
[16] C. J. Batty, E. Friedman, and A. Gal, Prog. Theor. Phys. Suppl. **117**, 227 (1994), and references therein.
[17] T. Yamada and Y. Yamamoto, Prog. Theor. Phys. Suppl. **117**, 241 (1994).
[18] C. J. Batty, E. Friedman, and A. Gal, Phys. Rep. **287**, 385 (1997).
[19] J. Dąbrowski, J. Rożynek, and G. S. Anagnostatos, Eur. Phys. J. A **14**, 125 (2002).
[20] E. Friedman and A. Gal, Phys. Rep. **452**, 89 (2007).
[21] J. Dąbrowski, Phys. Rev. C **60**, 025205 (1999).
[22] T. Harada, R. Honda, and Y. Hirabayashi, Phys. Rev. C **97**, 024601 (2018).
[23] R. Honda *et al.* (J-PARC E10 Collaboration), Phys. Rev. C **96**, 014005 (2017).
[24] M. Kohno *et al.*, Prog. Theor. Phys. **112**, 895 (2004).
[25] M. Kohno, Y. Fujiwara, Y. Watanabe, K. Ogata, and M. Kawai, Phys. Rev. C **74**, 064613 (2006).
[26] J. Hüfner, S. Y. Lee, and H. A. Weidenmüller, Nucl. Phys. A **234**, 429 (1974).
[27] E. H. Auerbach *et al.*, Ann. Phys. (NY) **148**, 381 (1983).
[28] T. Koike and T. Harada, Nucl. Phys. A **804**, 231 (2008).
[29] C. B. Dover and A. Gal, Ann. Phys. (NY) **146**, 309 (1983).
[30] H. Bandō, T. Motoba, and J. Žofka, Int. J. Mod. Phys. A **05**, 4021 (1990), and references therein.
[31] O. Morimatsu and K. Yazaki, Prog. Part. Nucl. Phys. **33**, 679 (1994), and references therein.
[32] A. Bohr and M. Mottelson, *Nuclear Structure* (Benjamin, New York, 1969), Vol. 1, p. 238.
[33] H. De Vries, C. W. de Jager, and C. de Vries, At. Data Nucl. Data Tables **36**, 495 (1987).
[34] H. Tyrén *et al.*, Nucl. Phys. **79**, 321 (1966); G. Jacob and Th. A. Maris, Rev. Mod. Phys. **38**, 121 (1966); **45**, 6 (1973).
[35] A. E. L. Dieperink and P. K. A. de Witt Huberts, Annu. Rev. Nucl. Part. Sci. **40**, 239 (1990).
[36] D. Vautherin and M. Brink, Phys. Rev. C **5**, 626 (1972).
[37] P.-G. Reinhard, in *Computational Nuclear Physics 1*, edited by K. Langanke, J. A. Maruhn, and S. E. Koonin (Springer-Verlag, Berlin, 1991), p. 28.
[38] S. A. Gurvitz, Phys. Rev. C **33**, 422 (1986).
[39] T. Harada and Y. Hirabayashi, Phys. Rev. C **105**, 064606 (2022).
[40] R. A. Eisenstein and A. Miller, Comput. Phys. Commun. **8**, 130 (1974).
[41] A. S. Rosenthal and F. Tabakin, Phys. Rev. C **22**, 711 (1980).
[42] R. A. Arndt *et al.*, computer code SAID, http://gwdac.phys.gwu.edu/.
[43] D. Marlow *et al.*, Phys. Rev. C **25**, 2619 (1982).
[44] T. Takahashi *et al.*, Phys. Rev. C **51**, 2542 (1995); K. Aoki *et al.*, *ibid.* **76**, 024610 (2007).
[45] P. B. Siegel, W. B. Kaufmann, and W. R. Gibbs, Phys. Rev. C **31**, 2184 (1985).
[46] R. J. Peterson, A. A. Ebrahim, and H. C. Bhang, Nucl. Phys. A **625**, 261 (1997).
[47] E. Friedman, EPJ Web Conf. **130**, 02005 (2016), and references therein.
[48] R. Michael *et al.*, Phys. Lett. B **382**, 29 (1996); R. E. Chrien *et al.*, Nucl. Phys. A **625**, 251 (1997).
[49] G. Backenstoss *et al.*, Z. Phys. A **273**, 137 (1975).
[50] C. J. Batty *et al.*, Phys. Lett. B **74**, 27 (1978).
[51] R. J. Powers *et al.*, Phys. Rev. C **47**, 1263 (1993).
[52] T. Harada, in *Proceedings of the 23rd INS International Symposium on Nuclear and Particle Physics with Meson Beams in the 1 GeV/c Region, Tokyo, March 1995* (Universal Academy Press, Tokyo, 1995), p. 211.
[53] Y. Yamamoto *et al.*, Prog. Theor. Phys. Suppl. **117**, 361 (1994), and references therein.
[54] M. M. Nagels, Th. A. Rijken, and J. J. de Swart, Phys. Rev. D **20**, 1633 (1979).
[55] T. Harada and Y. Hirabayashi, Nucl. Phys. A **829**, 100 (2009).
[56] T. Harada and Y. Hirabayashi, Phys. Rev. C **86**, 014606 (2012).

[57] J. Dąbrowski and J. Rożynek, Phys. Rev. C **23**, 1706 (1981).

[58] J. Mareš, E. Friedman, A. Gal, and B. K. Jennings, Nucl. Phys. A **594**, 311 (1995).

[59] J. P. Jeukenne, A. Lejeune, and C. Mahaux, Phys. Rep. **25**, 83 (1976); Phys. Rev. C **15**, 10 (1977).

[60] J. Dąbrowski and J. Rożynek, Acta Phys. Pol. B **14**, 439 (1983); Phys. Rev. C **78**, 037601 (2008).

[61] Y. Yamamoto *et al.*, Prog. Theor. Phys. Suppl. **185**, 72 (2010).

[62] R. Hausmann and W. Weise, Nucl. Phys. A **491**, 598 (1989).

[63] R. H. Dalitz and A. Gal, Phys. Rev. Lett. **36**, 362 (1976).

[64] A. Bouyssy, Nucl. Phys. A **290**, 324 (1977).

[65] C. B. Dover, L. Ludeking, and G. E. Walker, Phys. Rev. C **22**, 2073 (1980).

[66] N. Auerbach, Phys. Rev. C **35**, 1798 (1987).

[67] A. Gal and C. B. Dover, Phys. Rev. Lett. **44**, 379 (1980).

[68] A. Likar, M. Rosina, and B. Povh, Z. Phys. A **324**, 35 (1986).

[69] M. Kohno, Prog. Theor. Phys. **88**, 537 (1992).

[70] A. M. Lane and C. F. Wandel, Phys. Rev. **98**, 1524 (1955).

[71] J. Haidenbauer, S. Petschauer, N. Kaiser, U.-G. Meisner, A. Nogga, and W. Weise, Nucl. Phys. A **915**, 24 (2013).